Fast and Slow Flux Dynamics in Superconductors

A Magneto-Optical Imaging Study

Åge Andreas Falnes Olsen

Thesis submitted for the degree of Philosophiae Doctor
Department of Physics
University of Oslo
May 11, 2007

Preface

The 5 years of work that lead to this thesis have been rewarding in many respects. Most importantly, I have worked with colleagues both sociable and strong in physics, I have had the privilege to travel abroad, but first and foremost I have been able to learn interesting physics. Particularly in the past two years Daniel Shantsev has been a great motivator and discussion partner, and his comments on everything from physics to style of writing have been invaluable. Throughout my time at the University of Oslo my supervisor Tom Henning Johansen has contributed likewise: a deep insight into superconductivity and magnetism, and the willingness to share it, has been enormously important for me. Pål Erik Goa built the microscope that resolved single vortices: for nearly a year I worked very closely with him, and some of that work ended up in this thesis. It is not often one meets people as open and friendly as he is.

One of the stimulating parts of working in the Superconductivity group has been the many visits from guest researchers. I have been fortunate enough to work closely with some of them: Takayuki Ishibashi, Fabiano Colauto, and two of my Korean coauthors, Eun-Mi Choi and Hyonsook Lee. Also, the most important hardware in the group has been the coffee machine, around which Jørn Inge Vestgården, Øyvind Haugen, Grunde Løvoll (the only norwegian researcher I know who has published in Japanese - with some help from a translator...), and many others have gathered for a daily dose of discussions on wide ranging topics.

One more person deserves a special thanks: Harald Hauglin is the man who got me into superconductivity in the first place. He has always been willing to help when I have needed it, despite having a job outside the institute and a large family. His stamina, bordering on stubborness, have helped me overcome many hurdles. He also opened my eyes to the joy of building and designing simple mechanical and electronic gadgets. I think no black box remains black for long if you give it to Harald. In particular a long discussion on the contents of this thesis was very helpful.

The institute administration probably only hear from people when they are angry: after all an administration should be unnoticed when it works, but highly noticeable when it does not. I am nevertheless greatful for their help on the few occasions it has been necessary. Lastly, I would say that one of the most important support units at the institute is the mechanics workshop. The people working there are very helpful, and a lot of their work now stands in the lab I was using.

Of course, I have not been researching physics all the time. Michael Baziljevich offered me the opportunity to rediscover my childhood through choosing me to lead a Lego competition for young kids, as part of the annual Astrofestival (http://www.astrofestival.no). I have enjoyed it immensely: particularly shopping the prizes have been great! I have earned little money on that job, but a lot of Lego...

But I save the most stimulating part to the end. The best thing about doing low temperature physics is the virtually unlimited supply of liquid nitrogen. Here is a good tip: take

- 6 eggs

- 1 litre of cream

- $\approx 1/3$ kg sugar

- flavour (a few tablespoons of chocolate powder, vanilla or anything you fancy)

Whip eggs and sugar in a large bucket. Add the cream and flavouring and whip further. Then pour liquid nitrogen into the bucket while stirring vigourously - a little help is probably needed here. After less than 15 minutes you have a delicious ice cream! The recipe has been quality tested on my two daughters and my wife, all of them ice cream lovers, as well as countless children and parents visiting the University.

Contents

Chapter 1

Overview

This work presents experimental results on flux penetration into superconductors in two extreme dynamical regimes. The bulk of the work presented here relates to a particular type of flux instabilities which has become known as dendritic avalanches due to their peculiar, tree-like morphology when observed magneto-optically. They represent the fast extreme: when the instabilities develop they typically propagate at speeds of several 10's of km/s, involving large numbers of flux quanta. The slow extreme is represented by the observation of single flux quanta as they enter a superconductor: the process is observed on a microscopic scale in a small region, and involves the gentle motion of individual flux quanta as they are driven into the sample by the supercurrents.

The dendritic avalanches represent a severe challenge in high field applications of superconductors. The cost and complications involved in cooling superconductor magnets limit their scope of application to certain specialised cases requiring large fields, such as the plasma-stabilising magnets in the ITER fusion reactor under planning [1], the beam control fields in the Large Hadron Collider at CERN currently under testing, or high-field magnets used in Magnetic resonance imaging (MRI). Recently a test electromotor/generator based on superconductors has been shown to be reliable and efficient, albeit a commercial system is still some way into the future [2]. In all these applications flux instabilities must be avoided for a normal operation, and this is one reason there has been a strong interest in this phenomenon.

However, an equally powerful motivation for researchers is the many challenges involved in understanding the nucleation and evolution of the instabilities. They represent a highly complex, non-linear phenomenon arising

from the interplay between electromagnetic, thermal and pinning properties of superconductors, and particularly the dendritic avalanches are remarkably complicated structures. It is difficult *not* to be deeply fascinated by their very existence.

In this work I have used magneto-optical imaging, described in chapter 2, to study these avalanches in superconducting rings. After a description of the more regular superconducting electrodynamic behaviour in chapter 3, I close the introductory part of the thesis with a chapter on the dendritic instabilities (chapter 4).

This project started out as a project in single vortex imaging; for various reasons the direction of the project took an unexpected turn after a few years. The fact that the emphasis in the thesis is on flux instabilities does not reflect the work hours spent on the single vortex imaging project. However, at the end of the day it was the experiments on flux avalanches that brought most of the results worth reporting, and they therefore have a prominent role in this text.

Chapter 2

Experimental setup and data analysis

The experimental technique used in this work is magneto-optical (MO) imaging, which is a method for visualising magnetic fields using optical light. It is based on the Faraday effect where polarised light has its plane of polarisation rotated by a magnetic field. By placing a Faraday active sensor film close to the object under study, a detectable rotation is produced which can be utilized to deduce the magnetic field. The first to apply the technique to study superconductors was Alers [3] in 1957, who obtained a spatial resolution of some 0.25 mm. A significant improvement was achieved by Kirchner in 1967 [4] who reached a spatial resolution of a few μm. The technique was further refined and applied in studies on superconductors in the 1970's and 1980's (for a review, see [5]). A major breakthrough came when ferrite garnet films (FGFs) were introduced by Indenbom *et al* [6] in 1990, which allowed magneto-optics to be applied to the study of the newly discovered high-temperature superconductors because of their high sensitivity also at elevated temperature.

An attractive feature of MO imaging is its simplicity. With relatively inexpensive equipment and a simple set-up it is possible to measure the detailed surface distribution of magnetic flux over a sample wide area. Using a digital camera as detector one can collect and store data in a straight forward manner, and with a video camera it is also possible to obtain a high temporal resolution. Nevertheless, several flavours of more complicated setups have been developed over the years. For example, Wijngaarden *et al* [7] has developed a scheme (dubbed MO-ILIA) which allows bipolar sensitivity at video rate image acquisition: this is not so obvious in MO,
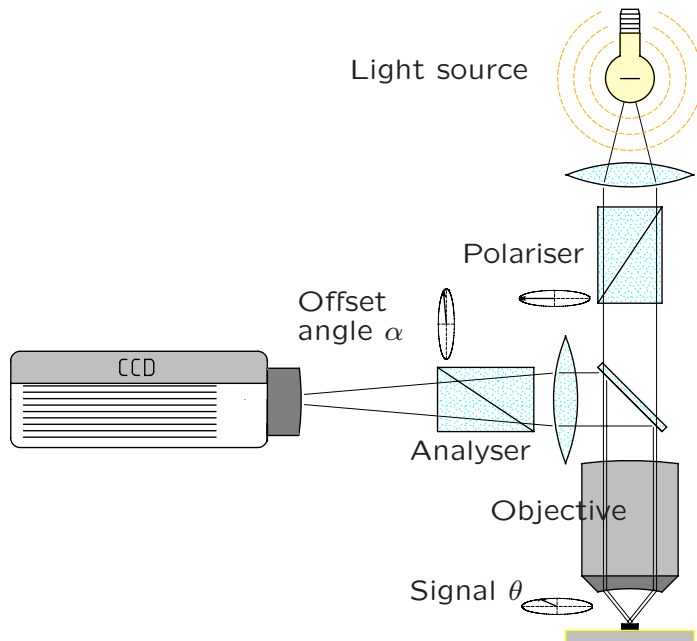
Figure 2.1: A sketch of a typical polarisation microscope used in magneto-optical imaging.

as will become clear later. A different example is the way Soibel *et al* [8] has pushed the limits of the field sensitivity to see tiny differences in flux density, on the order of μT, over large regions.

To realise the full potential of the technique is more challenging. In particular, the temporal response of the films are on the order of a few hundred ps [9, 10]. With a sophisticated detection system using lasers Leiderer *et al* [11, 12, 13] has exploited this extremely fast response to probe dynamics on the nano-second scale in superconductors.

2.1 Polarisation microscopy

The basic scientific instrument in MO imaging is the polarisation microscope. Figure 2.1 shows a sketch of such a microscope. Light from a powerful source, in our case a 100 W mercury lamp, is collimated by the first lens, after which the light passes through a polarisation filter to prepare a well-defined polarisation state. After passing through a beamsplitter the light is focused on the sample by the objective lens. The return light is reflected

in the beamsplitter towards a second polarisation filter, the analyser, and focused on a CCD chip. If this second polarisation filter is adjusted so that it blocks nearly all the light which emanates from the first filter, even quite small signals lead to a large change in the light intensity at the detector.

We can express the light intensity mathematically. Suppose the angle between the two polarisation filters is α, where the zero point is defined such that $\alpha = 0$ at full extinction. Suppose further that the sample imposes some small rotation θ on the polarisation state of the light beam. The light intensity at the detector is described by Malus law

$$I(x', y') = I_0 \sin^2(\theta(x, y) + \alpha) + I_b(x, y) \tag{2.1}$$

Here coordinates (x, y) refer to positions at the object, and are written to highlight that the quantities are position dependent. $I_b(x, y)$ is a background intensity which takes into account imperfections in the optical system and disturbances in the polarisation state which does not depend on the polarisation rotation at the sample. I_0 can be considered a normalisation factor, with $I_0 + I_b$ the total light intensity at full opening.

From equation 2.1 it can be deduced that for zero offset angle $\alpha = 0$, the intensity function is symmetric about $\theta = 0$, leaving the experimenter blind to rotation direction. With a non-zero α sensitivity to direction is accomplished, but at a cost in image contrast since the background intensity increases. Some insight may be gained by considering mathematically the contrast function between maximum and minimum signal from an object. This may be expressed

$$\begin{aligned} c &= \frac{I_{max} - I_{min}}{I_{max} + I_{min}} \\ &= \frac{\sin^2(\theta + \alpha) - \sin^2(\alpha)}{\sin^2(\theta + \alpha) + \sin^2(\alpha) + e} \end{aligned} \tag{2.2}$$

The constant e is here $e = I_b/I_0$ and is roughly equal to the extinction ratio of the entire microscope. It expresses the accumulated effect of optical imperfections in the system, and is typically around 10^{-3}.

Equation (2.2) is plotted in figure 2.2 for two different values of the signal θ, $\theta = 0,01^o$ and $\theta = 1^o$, and three values of the extinction e. For the small signal the contrast is symmetric about $\alpha = 0$ and the peak contrast is found for α between 1 and 2 degrees. For the large signal the contrast function is asymmetric about $\alpha = 0$, with a maximum close to full extinction and a minimum at an angle corresponding to the signal. If only a uni-directional sensitivity is desired, one should use $\alpha = 0$, but the adjustment is somewhat more difficult if one needs bipolar sensitivity.
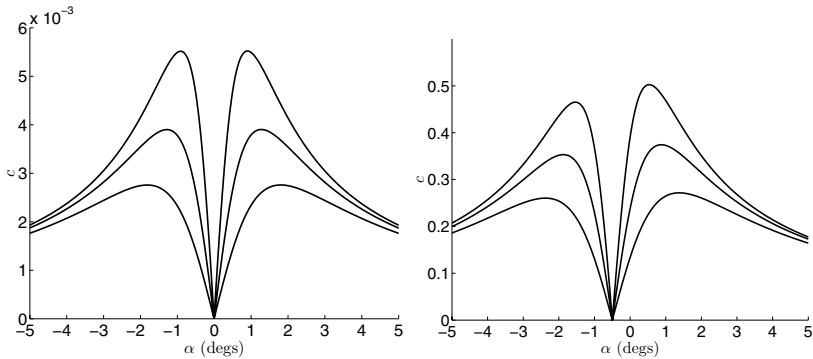
Figure 2.2: Plots of image contrast. Left plot shows a small signal of 0.01 degs, while the right plot represents a signal of 1 degs. The curves represent an extinction ratio e of 0.0005, 0.001 and 0.002 (from bottom to top).

This analysis excludes a background term in Malus law equation (2.1) dependent on α. This may arise if the sample is covered with some transparent material such as an object glass since part of the light incident on the top surface will be reflected without reaching the sample, adding an α-dependent background. However, one can mitigate this problem by covering the top surface with an anti-reflection coating.

In conclusion, there are several issues to be aware of when selecting the offset angle α. For a bi-directional sensitivity one must have $\alpha \neq 0$, but this can ruin some of the signal contrast. In practice it is usually a sensible strategy to check a test sample at several offset angles to try to find the best possible settings.

2.2 The FGF films

The ferrite garnet films (FGFs) used as indicators in magneto-optics are in-plane magnetised ferrimagnetic films with Curie temperature $\sim 350-400\,\mathrm{K}$. The films are typically $1-5\ \mu$m and grown on a substrate of Gadolinium-Gallium Garnet (GGG), which matches the structural and optical properties of the FGF fairly well. A mirror layer is usually deposited on the FGF. Considerable efforts have been invested in optimising the FGFs for use in magneto-optical imaging by changing the growth conditions, doping and so on; some more details on this may be found in the review by Jooss *et al* [5]. I will in this section focus on some basic physical properties of the films with relevance in this work.
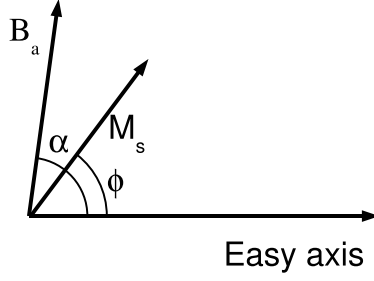
Figure 2.3: A simple model to describe the Faraday response of the FGFs. The easy axis lies in the film plane. In the absence of an applied field $\mathbf{B}_a$ the magnetisation vector $\mathbf{M}_s$ remains in this plane. With $\mathbf{B}_a \neq 0$ having an angle α with the plane, $\mathbf{M}_s$ rotates towards $\mathbf{B}_a$ and points in a direction with angle $\phi < \alpha$ with the plane.

The essential feature of the Faraday effect in the FGFs can be captured with a simple model depicted in figure 2.3. Consider a thin FGF of thickness d with infinite extension in the xy-plane. Polarised light propagates in the z-direction normal to the film plane. In the absence of an applied field $\mathbf{B}_a$ the magnetisation $\mathbf{M}_s$ is in the plane. If an applied field $\mathbf{B}_a$ is present with some angle α with the plane, $\mathbf{M}_s$ rotates towards the applied field. There are now two important contributions to the total energy; firstly, the magneto-static energy resulting from $\mathbf{M}_s$ and $\mathbf{B}_a$ not being aligned, and secondly the anisotropy energy which adds an energy cost in rotating the magnetisation away from the easy axis. Crucially, this energy balance leads to a gradual rotation of the magnetisation as the applied field is increased.

For a somewhat more formal analysis, one can write the energy density as

$$
\begin{aligned}
E_{ms} &= -\mathbf{B}_a \cdot \mathbf{M}_s + K \sin^2 \phi \\
&= -B_a M_s \cos(\alpha - \phi) + K \sin^2 \phi
\end{aligned}
$$

(2.3)

K is the anisotropy constant. The energy minimum as a function of ϕ defines ϕ; differentiating the above expression with respect to ϕ and putting $dE_{ms}/d\phi = 0$ yields the relation

$$
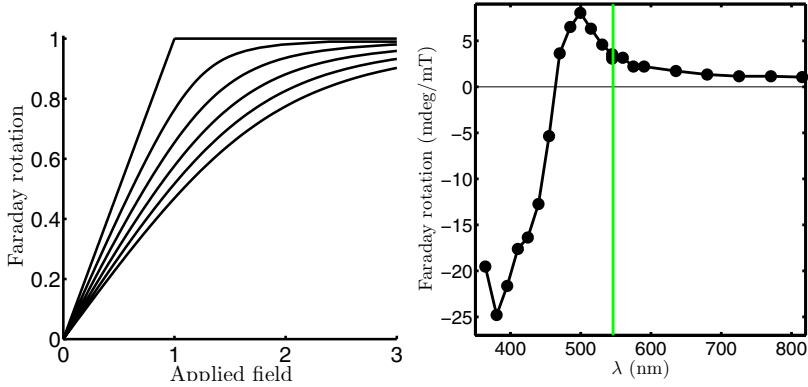\frac{B_z^{red}}{\sin \phi} - \frac{B_x^{red}}{\cos \phi} = 1
$$

(2.4)

7

Figure 2.4: (Left) plot of equation (2.6), in dimensionless units with the Faraday rotation measured in CM_s and the applied field in units of B_K. The Faraday rotation saturates towards some value, typically of the order of 0.01 deg/μm mT. An in-plane field lowers the sensitivity of the films and slows down the saturation, in the plot I show in-plane components 0, 0.2, 0.4, 0.6, 0.8 and 1. (Right) The spectral response of the Faraday rotation measured on one particular film, the green line showing the peak in the spectrum from Hg lamps. Data courtesy of Runar Wattum Hansen (unpublished)

The applied field B has been decomposed into its in-plane ($B_x = B\cos\alpha$) and normal ($B_z = B\sin\alpha$) components and expressed in reduced units of the anisotropy field $B_K = 2K/M$, which is constant if the magnitude of the magnetisation remains constant.

The Faraday rotation is proportional to the magnetisation component along the propagation direction of the light beam, and can be expressed as

$$\theta = CM_s \sin\phi \qquad (2.5)$$

C is the proportionality constant written explicitly for convenience. Equations (2.4) and (2.5) can be used to find the relation between the Faraday rotation and the applied field:

$$B_z^{red} = \frac{\theta}{CM_s} + B_x^{red}\tan\left(\arcsin\left(\frac{\theta}{CM_s}\right)\right) \qquad (2.6)$$

It is clear from this equation that if there is no in-plane B component the Faraday rotation is linear in the applied field provided it remains below the saturation value. The rotation then increases until the magnetisation

vector points along the z-direction, after which the rotation saturates and remains unchanged if the applied field is increased further. On the other hand, with $B_x \neq 0$ the Faraday rotation increases more slowly and only approaches the saturation value asymptotically. A plot of the behaviour is shown in figure 2.4 (a).

It should be emphasised that the Faraday response is close to linear in applied field provided the in-plane field component is much smaller than the anisotropy field, or if the rotation remains significantly smaller than the saturation value. Typically the anisotropy field in garnets is ~ 120 mT, and the saturation Faraday rotation up to $\theta = 0.02$ deg/ mT μm.

Equation (2.6) captures the essential features of the FGFs and explains why they are so useful in MO imaging. The Faraday rotation increases monotonically with applied field, and there exists a unique relationship between B_z and θ. However, the model leaves out some aspects of the garnets which are less beneficial for imaging. The in-plane magnetisation makes the films prone to domain splitting, which can be seen in polarisation microscopes as large triangular features of slightly different brightness. The domain boundaries, usually Bloch walls, move readily in response to changes in applied field, temperature and mechanical stresses. At cryogenic temperatures one can often observe domain wall motion for just a few kelvin changes in temperature, or a slight adjustment of the applied field. The ease with which the Bloch walls move, and the rather strong stray fields in their vicinity, have motivated the idea of using them to manipulate magnetic objects such as vortices in superconductors [14] and microscopic beads [15]. Perhaps the most important benefit in this arrangement is the ability to observe the manipulation in real time by fitting the system in a polarisation microscope.

However, the stray field near Bloch walls is rather more complicated than the simplest picture of a domain wall as a simple bar magnet suggests [16]. During observations of single vortices we observed many instances of an apparently paradoxical situation in which a dark domain wall appeared to attract bright vortices. The observation indicates that positive poles (the vortices) are attracted to positive poles (the Bloch wall, which is pointing downwards if it appears dark in images). It was shown in paper 4 that the paradox could be resolved by considering the effect of the nearby in-plane domains. Depending on the orientation of the in-plane magnetisation vector relative to the direction which the Bloch wall extends into, this may give an attractive force in a certain range between the vortices and the domain wall.

Mechanical strain can also affect the performance of the FGFs. This is particularly important in low temperature applications, partly because

thermal contraction induces strain at the FGF-GGG interface, and partly because of strain changes due to thermal contraction of any fixations between the FGF film and the cold finger. These thermal strains can affect the sensitivity of the FGF directly, but also give rise to depolarisation effects in the GGG substrate. The worst case scenario, which can be observed in many high-sensitivity films, is that the magnetisation flips out of the plane to form narrow labyrinthine bands of alternating magnetisation direction.

Finally, as shown in figure 2.4 the Faraday rotation is frequency dependent, with a strong peak in the rotation spectrum near $\lambda = 400$ nm. Unfortunately this is also a spectral region of strong absorption, and consequently not well suited for imaging. A second, smaller peak is found near $\lambda = 500$ nm at a wavelength with a high transmission. The figure also shows the wavelength of a strong peak in the emission spectrum of the mercury lamp used as a light source in the present work. It does not represent the optimal choice of wavelength, but I have been unsuccessful in the search for a usable, powerful light source with a spectral characteristic better matched to the Faraday rotation spectrum.

2.3 Measurement of the magnetic field

With a polarisation microscope and a usable FGF in place, one can image the magnetic flux distribution in a magnetic sample. The image intensity does not directly represent a pixel-wise map of the field, as is evident from Malus law equation (2.1). However, one can calibrate image intensity to magnetic field by combining Malus law and a relation between the magnetic field and the Faraday rotation, e.g. equation (2.6), see e.g. Jooss *et al* [5] for a detailed discussion. In the following I will outline the procedure used for the work in this thesis.

Firstly, a reasonable assumption is to limit attention to small angles in Malus law, in which case the sine factor can be expanded to first order yielding a quadratic relation between light intensity and rotation angle:

$$I(x', y') = I_0(\theta(B(x,y)) + \alpha)^2 + I_b(x,y) \qquad (2.7)$$

In order to have a more tractable analytic expression, I also linearise the Faraday response and write

$$\theta = 2V dB \qquad (2.8)$$

This approximation is commonly used; with the Faraday response written in this form the constant V is known as the Verdet constant, and d is

the FGF thickness. Combining the equations yields

$$I = a_2 B^2 + a_1 B + a_0 \tag{2.9}$$

where the constants a_i can be written as suitable combinations of V, d, I_b, I_0 and α. The second degree polynomial may be used to fit image intensity to field and thereby provide a calibration of the images. One can see from the equation that if $a_1 = 0$ the expression is symmetric in B and the field direction can not be deduced, which is the case for offset angle $\alpha = 0$.

The linearised Faraday response equation (2.8) should be used with care, as equation (2.6) and figure 2.4 clearly demonstrates. With no in-plane applied field the linear relationship exactly holds, but with increasing in-plane component the non-linear effects are increasingly important. With reference to figure 2.4 we can estimate that non-linear effects are important for $B_x \approx 0.4 B_K$ and $B_z \approx B_K$; with larger B_x the non-linearities become important at even smaller B_z. If we suppose a reasonable anisotropy field of $B_K \sim 120$ mT this corresponds to $B_z \approx 100$ mT and $B_x \approx 40$ mT.

Provided the Faraday rotations are small compared with the saturation value the linearity assumption is reasonable, but $V = V(B_x)$ depends on the magnitude of the in-plane field component. The dependence on the in-plane component is particularly troubling in the study of superconductors because magneto-optics is typically performed on fairly large, flat samples which expel magnetic flux. This will be explained in more detail in chapter 3; here it suffices to observe that the flux expulsion creates a considerable B_x which is in general unknown in experiments.

The presence of domains is also a challenge in intensity-to-field calibration since the domain walls move so readily in response to applied fields. Since the different domains appear as regions of different brightness even at zero applied field, this means the zero point in each pixel depends on whether a domain wall has passed the particular pixel or not. There are a few things an experimenter can do to reduce the domain splitting: ensuring that the edges of the FGF are smooth, ensuring that the the garnet is as unstressed as possible at low temperatures, and applying a weak in-plane field.

It is also necessary to compute a separate calibration curve in each pixel due to the uneven illumination in the field of view, and possibly also due to spatially varying material properties of the garnet itself or the GGG substrate. If the superconducting sample has a high transition temperature, one faces a trade-off between considering the temperature dependence of the Faraday rotation (which favours a calibration at the measurement temperature, but at a location far from the sample), and considering a spatially varying Faraday rotation (which favours calibration at the same location as
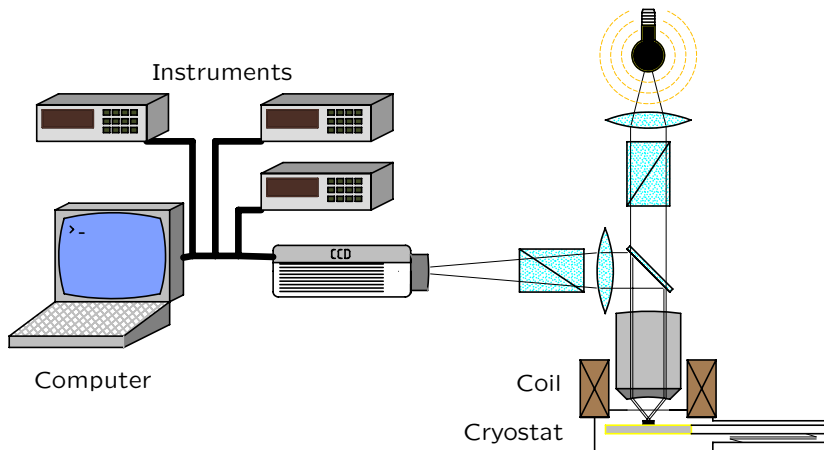
Figure 2.5: Instrumentation set-up

the sample, but above T_c). For the studies on MgB_2, which has a $T_c = 40$ K I have opted to calibrate at the measurement temperature.

2.4 Instrumentation

MO is flexible and does not need any sophisticated instrumentation. The most important data are the images of the distribution of the Faraday rotation, which rarely needs any complicated setup. However, in many cases it is convenient to use computers to log auxiliary data, and sometimes even to control some aspects of the experiments. In the experiments conducted for this thesis hundreds of images have been acquired, so a certain help from computers have greatly helped in a systematic acquisition and storage of data.

Figure 2.5 shows a sketch of the instrumentation set-up. The sample is mounted inside an optical flow cryostat from Oxford Instruments. It is possible to reach temperatures slightly below liquid helium with this equipment. The temperature is read and controlled by a temperature control unit, the Oxford Instruments ITC503. This unit can be controlled from computer via GPIB.

The coil current is supplied by a controllable power source, a Delta Electronica 700 W power supply capable of outputting up to 20 A/35 V or 10 A/70 V. The control voltage was supplied from a computer fitted with a card capable of outputting analogue voltages from DA converters with either 12 or 16 bit resolution. The coil current was monitored by
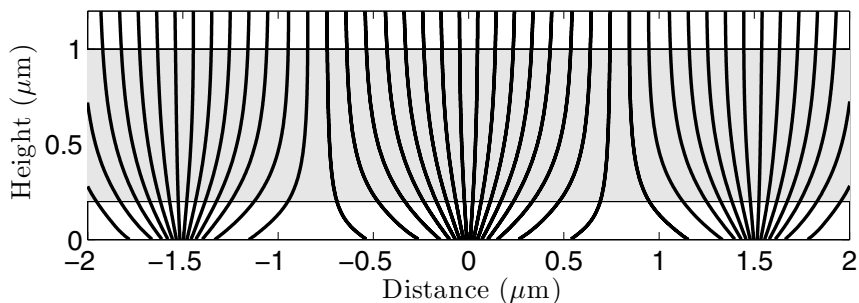
Figure 2.6: Just above the superconductor the stray field from vortex lines spreads out to form a uniform field less than a vortex spacing above the surface. The distances are measured in microns. The shaded area indicates a typical location of the FGF as the experiments were conducted on NbSe$_2$. The field from the vortices have been approximated with a monopole field (see Carneiro and Brandt [17]) assuming a penetration depth $\lambda = 100$ nm, roughly corresponding to NbSe$_2$

reading a voltage signal from the power supply proportional to the output current. While this is quite simple to do from a data acquisition card in the computer, it was often more convenient to use an externally controllable voltmeter: this gives more reliable readings with higher resolution, albeit at a cost since the voltage readings take much more time this way.

Finally, the CCD cameras used are a Hamamatsu C3987 digital video camera (vortex entry paper, paper 3) and a Retiga Exi from QImaging (in the MgB$_2$ ring papers, papers 1 and 2). The latter camera has good sensor quality and a very flexible computer interface. There are LabVIEW drivers available which makes it quite simple to integrate image capture with other auxiliary readings (of temperature, coil current etc). The actual programming has been performed in LabVIEW.

2.5 High resolution imaging

The papers 3 and 4 present experimental images acquired with a custom built polarisation microscope with very high resolution. In MO imaging a high resolution is challenging for two main reasons. Firstly, the magnetic field modulation in the vicinity of two magnetic objects which are close together is smeared out on a length scale similar to the separation of the objects, illustrated in figure 2.6. The figure shows field lines just above the

surface of a superconductor from individual vortices. [1] Also shown is the typical location of a thin FGF used for single vortex observation. It is clear that the signal decays quickly above the surface, and for even the relatively thin film of 0.8 μm most of the signal is picked up in the lower part of the film.

A second challenge is the trade-off between a high NA necessary to see the tiny objects, and a stronger depolarisation induced by the same high NA. Some depolarisation, or change in the initially well prepared polarisation state, is inflicted on the light whenever it refracts through a boundary or is reflected off a surface. This effect is strongly dependent on the angle of incidence as well as the angle between the polarisation vector and the plane of incidence. When a high NA objective lens focuses the light, the light meets surfaces at quite large angles, and thus experiences a relatively large depolarisation.

Despite the challenges involved, Goa *et al* [21] managed to visualise single vortices in superconductors (see chapter 3) using MO, a feat which was later reproduced by Terao *et al* [22]. These objects typically have a lateral extent similar to the wavelength of light, but by constructing a custom built microscope it was possible to resolve these tiny magnetic objects. The sketch of the principle shown in figure 2.1 remains valid, but the polarisation filters are calcite crystals with extremely large extinction ratios ($10^{-6} - 10^{-5}$), the beamsplitter is a special configuration known as a Schmidt beamsplitter which reduces angles of incidence on reflective surfaces and at transmission boundaries. Finally, a high quality objective lens with NA = 0.5 is used.

While this optimisation of the optical components is crucial, two further tricks are required in order to see the vortices. Firstly, the indicator film, which is *not* covered with a mirror, is securely fixed on the sample using aluminium sticky tape. Since the FGF is free of a mirror layer, one can use the dark and bright bands caused by interference between light reflected from the sample surface and the bottom of the indicator film as a guide to the distance between sample and indicator film. This allows one to ensure that the distance between indicator and sample is as short as possible.

Secondly, the objective lens is moved inside the vacuum chamber surrounding the cold finger. This contrasts the typical low-temperature set-up where the cryostat and the microscope are separated and the observations are made through a small glass window in the cryostat. This eliminates an important source of depolarisation.

---

[1]see chapter 3 for an introduction on superconductivity, and Pearl [18], Huse [19], Marchetti [20] and Carneiro and Brandt [17] for details on the vortex structure near interfaces.

14

Despite the efforts in optimising the performance of the microscope and placing the indicator very close to the sample, there are so far only two superconductors (NbSe$_2$ and Nb) where vortices have been successfully observed. One reason is that one needs the sample to behave as an optical mirror; a second reason is that these superconductors have beneficial material properties for this type of imaging. Tokunaga *et al* [23] recently presented an improvement on the setup by covering the indicator film with a Nb mirror. The Nb mirror is itself superconducting and vortices in a sample below will generate a field that the Nb film bundles into a vortex, which is then observed in the microscope. The authors suggested this trick may extend the usefulness of the technique.

2.6   Data analysis

I have used Matlab extensively for quantitative analysis of images. The image treatment toolbox in Matlab contains a host of functions convenient in such work. The scripting feature in Matlab also makes it simple to apply treatment or analysis to many images.

For automated conversion from intensity units to magnetic field Matlab was used to read calibration images and a log file containing values of the applied field corresponding to each image, and then computing a least squares second degree polynomial fit of field vs intensity in every pixel in the images. The fitting coefficients were then used to convert the intensity images to field maps.

When the map of magnetic field is available, we can use it to extract the underlying current distribution. An example of this operation is shown in figure 2.7. The procedure is based on the Biot-Savart law which relates a magnetic field distribution to a current distribution:

$$\mathbf{B}(\mathbf{r}) = \frac{\mu_0}{4\pi} \int_V \frac{\mathbf{J}(\mathbf{r}') \times (\mathbf{r} - \mathbf{r}')}{|\mathbf{r} - \mathbf{r}'|^3} d^3 \mathbf{r}' \qquad (2.10)$$

The integration is carried out over the current filled volume. To extract the current distribution from this equation requires an inversion which is not trivial, but we can make some simplifications which eventually allows us to perform a highly efficient inversion. The scheme is due to Roth *et al* [24].

In magneto-optics, we are interested in a 2-D current and field distribution, with only the normal-component of the field measured. If we assume there are no current sources or sinks in the image, i.e. we see the entire sample in our field of view, we have $\nabla \cdot \mathbf{J} = 0$ everywhere. When this holds, the current may be expressed via a scalar variable g, known as the local
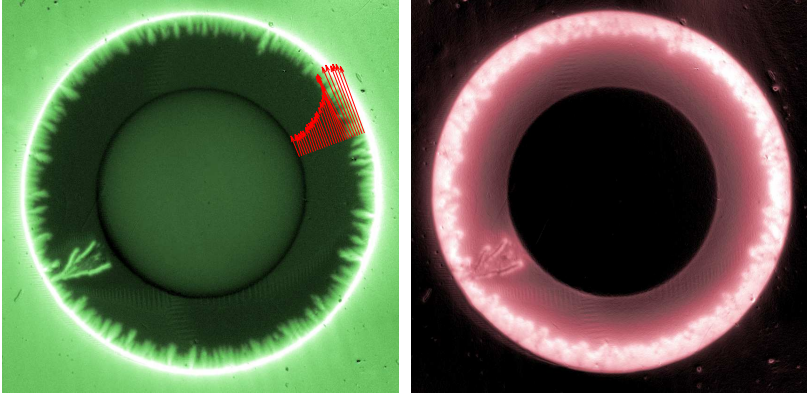
15

Figure 2.7: An experimental magnetic field map with current arrows superimposed, and the corresponding current density map obtained from inversion of the Biot-Savart law

magnetisation, by $\mathbf{J} = \nabla g \times \hat{\mathbf{z}}$. See e.g. Brandt [25] for a rather detailed discussion of this scalar function in the context of flat superconductors. We can now rewrite the Biot-Savart law as

$$B_z(\mathbf{r}) = \frac{\mu_0}{4\pi} \int_{z'} \int_{r'} \nabla g(\mathbf{r}', z') \frac{(\mathbf{r} - \mathbf{r}')}{((\mathbf{r} - \mathbf{r}')^2 + (z - z')^2)^{3/2}} d^2\mathbf{r}' dz' \qquad (2.11)$$

Here $\mathbf{r}$ is restricted to the plane and the normal component z has been written out explicitly. In this form the expression is well suited for a Fourier transform, since the integration with respect to $\mathbf{r}$ is a convolution of two functions ∇g and $f = f(\mathbf{r}, z)$. Finding an analytic expression of the Fourier transforms is not trivial; however, an analytic expression can be found, and with the additional assumption that the current distribution is restricted to a thin layer with thickness d, we can write for the Fourier transform of g

$$\tilde{g}(\mathbf{k}) = \frac{2}{\mu_0 dk} \tilde{B}_z(\mathbf{k}) \qquad (2.12)$$

The advantage of rewriting the original Biot Savart law this way is that we can apply the highly efficient FFT transform on the field maps, divide by k, and an inverse FFT yields the real space g-function. The current density is then found by differentiating g; $\mathbf{J} = [\partial g/\partial x, -\partial g/\partial y]$.

The algorithm then essentially consists in four steps:

- Compute the FFT of the field map

- Build the k-vector at every position

- Compute g and differentiate

- Inverse transform the result to obtain the current distribution

A second interesting algorithm which can be used to extract the locations of individual vortices is described in appendix A.

Chapter 3

Magnetic flux in superconductors

The purpose of this chapter is to introduce some basic concepts in super-conductivity which are relevant in this work, and to discuss two important aspects of the electrodynamics of superconductors. The first is at the microscopic level, where I am interested in the quantum of flux, Φ_0, and how edges may affect its motion during entry into superconductors (section 3.2). The second is to introduce the basic electrodynamic properties of flat superconducting rings (section 3.4).

The study of rings and tubes may seem rather esoteric. Nevertheless, these geometries have some important applications in experimental research and material charaterisation. The most striking historical example is the confirmation of magnetic flux quantisation in superconductors. Doll and Näbauer [26] used a highly sensitive technique for measuring the magnetic torque on a micron-sized Pb tube, while Deaver and Fairbank [27] measured the flux contained inside a Sn tube using an ingeneous set-up of pick-up coils. Both groups found that Φ inside the tubes increased in quantised units, with the size of the units being $\Phi_0 = h/2e$. In fact, their discovery that the unit of flux was $h/2e$ instead of h/e was taken as vindication of the existence of Cooper pairs in superconductors [28].

Rings and tubes also have some technological interest. One example is in material characterisation, where one wants to determine J_c, the maximal current which the superconductor can sustain in the presence of an applied field. J_c is often deduced from magnetisation measurements, and rings have a particularly beneficial property in this respect because the magnetic moment of a ring shows a distinct crossover when the applied field reaches the

level where the ring current has saturated. This crossover is seen as a peak in a plot of dM/dB_a vs B_a. There is no such distinct crossover in alternative simply-connected geometries such as a disk: such a determination of J_c is performed in practice in e.g. ref [29]. B_p can also be computed as a function of J_c for a ring with finite thickness [30]. Rings and tubes are also recurring shapes in technological applications of superconductors such as permanent magnets [31], superconducting bearings [32] and SQUIDs.

3.1 Superconductivity rudiments

Superconductors expel magnetic field. In the Meissner state the expulsion is complete, with currents flowing near the surface of the material in such a way as to exactly cancel the applied field. In a bulk superconductor the screening defines the two fundamental material constants in superconductivity: the penetration depth λ and the coherence length ξ. Physically, one can think of λ as the distance that magnetic fields penetrate, or alternatively the narrow region near the surface where the screening currents flow. ξ can be thought of as the distance along which the density of superconducting electrons decay near a surface. The exact values are properties of specific materials. In some cases λ can be greater than ξ, in some cases the opposite is true. Of fundamental interest is the special case when $\lambda = \sqrt{2}\xi$, which demarcates two profoundly different types of superconductors. This thesis deals exclusively with type-II superconductors, for which $\lambda > \sqrt{2}\xi$.

When this condition is fulfilled, it was realised by Abrikosov [33] that flux will penetrate superconductors in discrete quanta, later known as vortices or flux lines, if the applied field exceeds a certain minimum field B_{c1}. The importance of this fundamental discovery was highlighted by his share in the 2003 Nobel prize in physics. Each vortex carries one flux quantum, $\Phi_0 = h/2e = 2.07 \cdot 10^{-15}$ Wb. The core is a cylindrical region of size $\sim \xi$ where superconductivity is suppressed; here a rather high magnetic field is found which decays fast with decay length $\sim \lambda$ as one moves away from the core. From the current circulating a vortex one can deduce an expression for the mutual vortex-vortex interaction; it is repulsive but decaying exponentially at long distances. If, as Abrikosov did, one considers only this mutual interaction and also assumes an isotropic superconductor, a collection of vortices will form a hexagonal lattice structure.

The existence of this lattice was decisively confirmed experimentally about a decade after they were predicted theoretically. Traüble and Essmann [34], and independently Sarma and Moon [35], succeeded in refining the Bitter decoration technique [36] sufficiently to visualise vortices for the first time. This technique consists in sprinkling a magnetic structure with
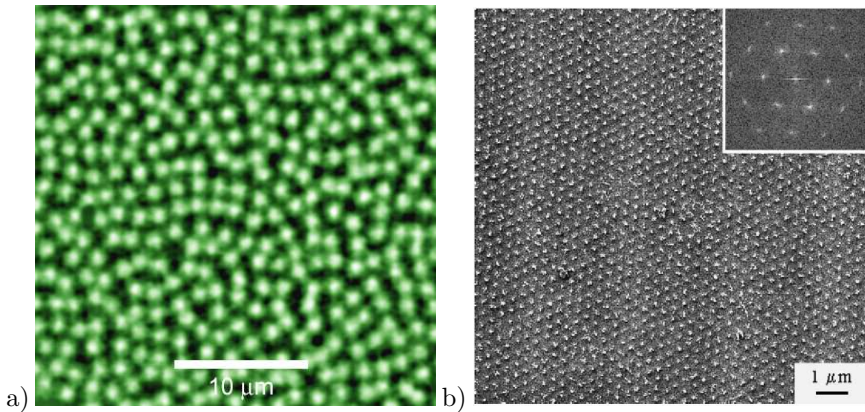
Figure 3.1: Images of vortices in superconductors. (a) MO image obtained on $NbSe_2$. Taken by Pål Erik Goa. (b) Decoration image on MgB_2 (from Vinnikov [40])

nanometer-sized ferromagnetic particles, which tend to cluster on the surface near strong field gradients. Observing the pattern of these ferromagnetic particles then reveal the magnetic patterns at the surface. While the technique provides quite high spatial resolution over a very large area, an important drawback is its one-shot nature: applied to superconductors one will have to heat the sample to room temperature to observe the actual patterns on the surface.

Since then a range of other techniques have been adapted to see the vortex lattice in real space or the reciprocal lattice: neutron scattering, muon scattering, Lorentz microscopy [37, 38], Hall sensors, magnetic force microscopy (see Bending [39] for a review), and most recently magneto-optical imaging [21, 22, 23]. Figure 3.1 shows images of the vortex lattice using the Bitter decoration technique and MO imaging: the MO image was obtained in our group using a custom built polarisation microscope. The image shows vortices in $NbSe_2$ at an applied field $B = 0.6$ mT. The decoration image is taken from Vinnikov [40], showing the vortex lattice in MgB_2.

The dynamics of the vortex lattice determines the electro-dynamic properties of the superconductor, and hence an understanding of the behaviour of the vortex lattice is paramount since most of the prospective applications of superconductors involve high currents and magnetic fields. The basic challenge in combining high dissipation free currents and high magnetic fields is the fact that current will subject a vortex to a force, which

will induce motion of the vortex, and this motion generates an electric field which opposes the driving current. One could hence formulate the basic engineering problem in superconductivity as designing the optimum pinning strength in materials to ensure vortices remain motionless even in the presence of large current densities.

Fortunately, vortices are to a greater or lesser extent pinned by the superconductor, by forces exerted from crystal defects, surface texture, or various other sources. One reason that the structural properties of the lattice are interesting is that the degree to which a vortex lattice is pinned is to some extent reflected in its structural properties. This can be appreciated by a simple physical picture (due to Larkin and Ovchinnikov [41]). A perfect and stiff vortex lattice moves collectively, even if some of the individual vortices experience a small pinning force: because of the stiffness of the lattice the other vortices drags them along so the overall motion remains unimpeded. On the other hand, if the lattice stiffness is reduced (for example by diluting the density of vortices) or the pinning strength increased, the lattice may break up or experience severe shear, since some groups of vortices may become stuck at pinning sites while others are free to move. As a result, a better pinned lattice will typically be more disordered.[1]

The phenomenological critical state model, originally due to Bean [52] and Kim [53], has proved to be a highly effective way to describe the macroscopic electro-dynamic behaviour of superconductors without considering the vortex lattice in all its microscopic detail. The model is based on two assumptions:

- the material can only carry a limited current, the critical current J_c, in the presence of a magnetic field

- this critical current will always flow where field has penetrated

The latter assumption describes the fact that the superconductor will screen flux as well as possible: with a maximum current in the flux penetrated region the extent of that region is minimal, and hence the screened region is as large as possible.

The critical state has an intuitive microscopic interpretation. Vortices remain motionless until a driving force (typically the combination of current and interactions with other vortices) exceeds a minimum value, after which they move until (i) the driving force is reduced to below the critical level, or

---

[1]The structural properties of the vortex lattice are much more involved, it has been explored extensively in the literature revealing for example different glassy phases of the lattice [42, 43, 44], pinning induced structural defects, [45, 46, 47, 48], and inferred annealing processes from transport studies [49, 50, 51].

(ii) they encounter a stronger pinning site. The macroscopic critical current is then simply the minimum current required to induce vortex motion, and captures the accumulated effect of all possible pinning mechanisms, disorder in the vortex lattice induced by frustration forced upon it by field gradients, and so on. Increasing the applied field on a critical state superconductor lead to super-critical current for a brief time, rearranging the vortices in such a way that the critical state is re-established.

The critical state is a metastable state. Because the current is always at its critical value in the flux penetrated part of the superconductor, even the feeble thermal excitations can be enough to trigger small scale vortex motion. The consequence of this thermal motion is to induce a small electrical resistivity, and can be seen in e.g. magnetisation experiments where the magnetisation of a superconductor slowly decays in time. The effect was discovered in low-T_c materials in the early 60's and was described by among others Anderson and Kim [53] as a result of thermally driven flux motion. One may think of this as an activation process, where vortices trapped in a potential U can escape due to thermal excitations at a rate $r \propto \exp -U/kT$. With the discovery of high-T_c materials the phenomenon received increased attention because it is typically more pronounced in those materials than in the low-T_c superconductors. This is only partly due to the higher temperatures involved [54]: often the activation energy U is also smaller in high-T_c materials.

Several theoretical frameworks have been established to describe flux creep. I will not delve into the details in this work, it suffices to observe that the electric field resulting from the moving vortices depends on the current in a highly non-linear way. One frequently used relation is

$$\mathbf{E} = E_c \left(\frac{J}{J_c} \right)^n \hat{\mathbf{J}} \tag{3.1}$$

with $n = U/kT$ and $\hat{\mathbf{J}}$ the unit vector along the current. In general E_c, J_c and n all depend on the magnetic field and the temperature. Small n gives strong creep, while in the limit $n \to \infty$ U dominates over temperature fluctuations completely, and there is no thermally activated creep.

In this thesis equation (3.1) is exclusively used as a tool which simplifies computations. In fact, for MgB$_2$ thin films n can be very large, Thompson *et al* [55] found $n = 78$ at $T = 25$ K and $B = 1$ T. At lower temperature and field the value would be even larger. Along with the fact that the experiments described here typically takes only a few minutes to complete, it should be expected that creep effects can be safely ignored. In simulations I will use a sufficiently large n that it does not affect the current and field distributions significantly.

I close this section by stressing that the above treatment is rather simplified and superficial. Since the pinning forces encompass a large number of microscopic forces, the critical current J_c is influenced by numerous factors. It not only depends on the specific material, but also on sample fabrication and quality, geometry (e.g. surface steps, deliberately engraved holes or grooves), and sample treatment (e.g. irradiation, heat treatment, or tiny magnetic structures on the surface [56, 57]). The vortex-vortex interaction further complicates the dynamics of the lattice, because it is strongly modified by the superconductors crystal structure and geometry. For example in anisotropic materials one can find square or rectangular lattices [58], or chains as observed in the $Bi_2Sr_2CaCu_2O_{8+\delta}$ and $YBa_2Cu_3O_{7-\delta}$ high-T_c materials [59, 60, 61, 62].

3.2 Vortices near edges

It was mentioned during the brief description of single vortex MO imaging (section 2.5) that the field lines from single vortices "spread out like a mushroom", in the words of Pearl [18]. In the present work this observation is only relevant as a technical difficulty in observing the vortices[2]. However, edges are also important for the global electrodynamic properties of superconductors by acting as barriers to vortex entry, either via an attractive force between the edge and the vortex known as the Bean-Livingston barrier [63], or via a macroscopic energy barrier known as the geometric barrier [64].

Physically one can think of the geometric barrier as arising from the way field lines curve around edges of finite thickness superconductors [65]. Initially vortices nucleate at the corners, being dragged into the sample and extended as the applied field increases, until the two ends originating at the edge meet and form a single vortex spanning the sample from top to bottom. At this point the vortex contracts and, if the pinning force is weaker than the Lorentz force from the Meissner current in the superconductor, moves quickly to the central region of the sample. Exit of vortices, however, is unaffected, and hence this barrier can give rise to magnetic hysteresis in completely pin-free superconductors.

In paper 3 I present a short study on vortex entry into $NbSe_2$. This is a weak pinning superconductor, and previous work has shown that the current profiles and field distributions in specimens of this material may

---

[2]But obviously this does not mean that the effect is unimportant: the long range interactions that result affect the structure of the lattice and the motion of individual vortices
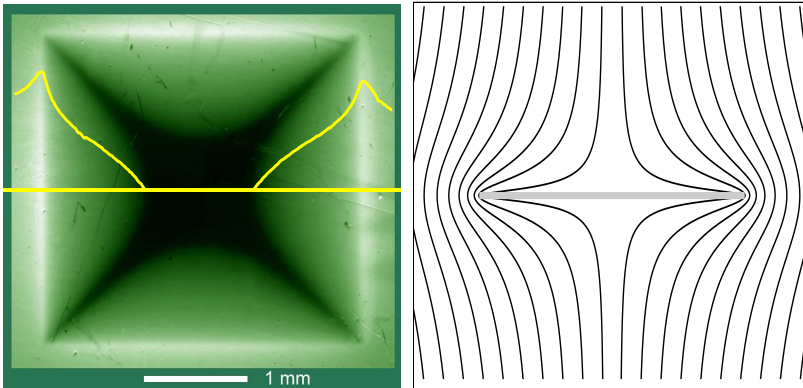
Figure 3.2: (Left) MO picture of a $YBa_2Cu_3O_{7-\delta}$ thin film in the critical state. The yellow curve shows intensity profile along the straight, yellow line. (Right) Side view of the field lines around a critical state slab, highlighting the flux expulsion from the interior and the concentration of flux lines at the edges.

be controlled by the geometric barrier [66]. With the single vortex microscope we were able to resolve vortices as they enter at an edge, displaying a narrow band there which vortices quickly move across once they have nucleated. Such a band can arise from the combined effect of pinning and the geometric barrier: qualitatively the observations are in line with a theoretical treatment by Elistratov *et al* [67], although a quantitative comparison with the theory was not conducted due to lack of sufficient experimental data. Not mentioned in the paper is a comparison of our experimental profiles on a thin $NbSe_2$ sample with calculated flux profiles assuming a weak pinning superconductor taking into account the geometric barrier [65]. The calculated profiles show a narrow band with large magnetic field very close to the edge, a flux-free band further away, and a gradual increase in field value towards the center of the specimen. The vortex free band decreases with field. All these features are observed in paper 3.

3.3 Flat superconductors in perpendicular fields

In a flat superconductor the basic tenet of the critical state model remains valid, namely that the current is maximal where flux has penetrated the sample. However, some special features of the current and flux distributions arise which are purely due to geometry. The effect on the flux profile is

shown in figure 3.2. The sample was cooled through T_c in zero applied field, after which the field was ramped up until magnetic flux penetrated a significant length into the sample. The applied field is directed out of the paper plane in the figure. The image shows clearly that magnetic flux is concentrated near the sample edges, and decaying in a non-linear fashion to zero at the flux front inside the superconducting material. This should be contrasted with the linear decay predicted for a semi-infinite slab, which can be seen from the Maxwell equation $\nabla \times \mathbf{B} = \mu_0 \mathbf{J}$ which becomes $dB/dx = \mu_0 J$ in the slab case.

The sharply peaked edge field stems from the fact that current in the superconductor, regardless of whether it is a transport current or a shielding current, generates stray magnetic fields in the vacuum outside the sample. This stray field adds up at the edges to give a strongly enhanced field there. In the Meissner region the stray field leads to an appreciable current [68, 69, 70] necessary to cancel the field there: this is in contrast to the case of a semi-infinte superconductor where there is no current in the flux free part.

There exists a unique relationship between the flux penetration length l, the applied field B_a, and critical current J_c. For flat superconductors this is not trivial to find: nevertheless, it is possible [69, 70] to obtain an analytic expression relating l, B_a and J_c in the case of an infinitely long strip with thickness d, width w, $w \gg d$:

$$B_a = \frac{\mu_0 J_c d}{\pi} \cosh^{-1} \left(\frac{w}{w - l} \right) \qquad (3.2)$$

This expression allows a precise and convenient determination of the critical current from magneto-optical images. The great advantage is that one does not need to calibrate image intensity to field, and hence does not need to take into account the in-plane components of the stray field. An additional advantage is conferred by the fact that the expression only involves the ratio w/l, and hence relating image pixel size to true length scales is unnecessary. A more involved, but also more precise, procedure which measures the annihilation zone position after a ramp up-ramp down cycle is described by Baziljevich *et al* [71].

While equation (3.2) is deduced under the assumption of an infinitely long strip, the expression is useful also in realistic sample geometries. On the other hand, one can calculate the flux and current distributions in much more complicated cases numerically. In particular, a general scheme developed by Brandt and others [72, 73, 74, 75, 76, 77, 78] allow calculations of the electrodynamics for more complicated cases such as disks, rectangles, or specimens with a finite thickness, as well as simulations of creep effects.

Most significant in this work is the fact that it also allows calculations on superconducting rings, which were needed in paper 2. The next section explains the procedure in some more details.

3.4 Rings and tubes

While superconducting rings and tubes only represent special cases of what was discussed in sections 3.1 and 3.3, the central hole or bore gives rise to some peculiar effects. Furthermore, it also makes the theoretical analysis more difficult and no analytic models have yet been developed, albeit the analogous problem with two co-planar strips connected at infinity has received some attention [69, 79]. However, it is possible to work with numerical calculations and find the evolution of the current and field distributions during a ramp of the applied field. I here follow Brandts scheme [76] and work with the magnetic potential $\mathbf{A}$, related to $\mathbf{J}$ via $\nabla^2\mathbf{A} = \mu_0\mathbf{J}$. Since the current in this case is distributed in a volume, the solution is written as an integral over the current distribution,

$$\mathbf{A} = \frac{\mu_0}{4\pi} \int_V \frac{\mathbf{J}(\mathbf{r}')}{|\mathbf{r} - \mathbf{r}'|}d^3r' + x\mathbf{B}_a \qquad (3.3)$$

For a cylindrically symmetric superconducting sheet with an applied field in the z-direction, both $\mathbf{A}$ and $\mathbf{J}$ has only an angular component, and the problem is essentially one dimensional. Equation (3.3) is written

$$A = \mu_0 \int_S Q(r,r')dJ(r')dr' + \frac{r}{2}B_a \qquad (3.4)$$

the integral being carried out over the sample area. The kernel is most simply expressed as

$$Q(r,r') = \frac{1}{2\pi} \int_0^\pi \frac{r'cos(\phi)}{\sqrt{r^2 + r'^2 + 2rr'cos(\phi)}}d\phi \qquad (3.5)$$

Equation (3.4) can be rewritten using $\nabla \times \dot{\mathbf{A}} = \nabla \times \dot{\mathbf{J}}$ and the creep law equation (3.1), and inverted. The result is an equation of motion for the current [76, 77]

$$\dot{J}(r) = \frac{1}{\mu_0} \int_{r_0}^{r_1} Q^{-1}(r,r')\left(J(r')^n\frac{E_c}{J_cd} - \frac{r}{2}\dot{B}_a\right)dr' \qquad (3.6)$$

This equation can be solved numerically. The time integration is straight forward. However, one needs a discretised version of the kernel and current.
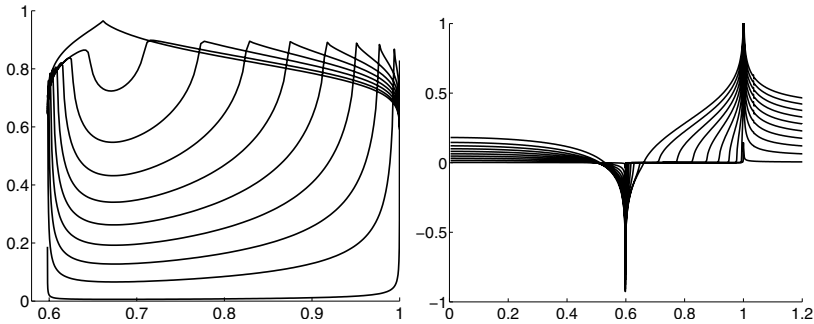
Figure 3.3: Computed current and field profiles in a flat, superconducting ring in the critical state, creep exponent is $n = 30$, and a Kim model field dependent critical current. The ring dimensions have been chosen to coincide with the rings studied in papers 1 and 2

With due attention to the choice of grid, and some careful tuning of the singular values in the integrand in equation (3.5) when $r = r'$, the computation is stable and accurate. The way we performed the kernel tuning is explained in paper 2.

The result of a calculation is shown in figure 3.3. When the applied field is ramped from 0 screening currents start to flow in the ring. The stray field from these currents generate a strongly peaked field at the outer edge similar to that observed for flat, simply-connected samples, see e.g figure 3.2. At the inner edge the stray field adds up to a sharply peaked *negative* field, leading to the penetration of anti-flux from the inner edge. Before the two flux fronts meet there remains a Meissner region in the center of the superconducting material where an appreciable non-zero current is flowing. At some applied field, the field of full penetration B_p, the two flux fronts meet at a radius r_p. At this point the current is maximal in the entire ring, and results in a crossover in its magnetic moment.

The radius of full penetration and the field of full penetration can be calculated from [76]

$$\frac{B_p}{\mu_0 J_c d} = \max\left(\frac{2}{r} \int_{r_0}^{r_1} Q^{-1}(r, r') dr'\right) \tag{3.7}$$

The calculation can be carried out analytically in r' first, which removes the singularity in $Q(r = r')$. The resulting integrand has a singularity for $\phi = \pi$, but the integral is still well defined.

The flux expulsion in flat superconductors in general also has the conse-

quence that there is a substantial in-plane field B_r near the superconducting material. It was mentioned in section 2.3 that such an in-plane field affects the sensitivity of the indicators used in MO imaging, and it thus represents a source of systematic error in image intensity to field calibration. This is particularly relevant for paper 2 where we measured the flux in a large area. However, most of the region where we measure the flux is within the central hole of the ring, where the in-plane component is mostly rather small. In fact, the worst case is found at the surface of the superconductor in the regions where J_c flows, where the B_r can be expressed as $|B_r| = \mu_0 J_c d/2 = 10$ mT for the ring used in the paper. This value should be compared with the value $B_K = 120$ mT for the anisotropy field (see section 2.2), and it is clear from the plots in figure 2.4 that we may safely disregard this source of error.

An analogy for rings is found in a superconducting strip with an applied transport current [68, 69, 72]. In such a case the current is distributed such as to screen the interior of the specimen from the stray fields. The stray fields combine at the edges, leading to flux penetration in a critical state fashion, with flux of opposite polarity penetrating from the two edges. With only a transport current present the flux profiles are symmetric about the center of the strip, but if the transport current is combined with an applied field the distribution becomes asymmetrical [69, 70] and resembles the ring current distribution shown in figure 3.3.

Chapter 4

Flux avalanches

The critical state description presented in the previous chapter is a quasi-static, global description. Any increase in applied field, or change in transport current, is accompanied by a redistribution of the flux in the superconductor to accomodate the new situation. The exact manner in which this redistribution happens was not considered, but it is simplest to think of the process as a smooth and instantaneous response to changes in the external conditions. In fact, the slow drizzle of vortices down the flux gradient does not proceed in a uniform way, but via avalanches whose sizes can span many orders of magnitude. In the present context the experiments by Field *et al* [80] is particularly interesting since they used a superconducting tube to measure how flux entered the central hollow region. Later an extensive research effort has been put down to investigate these avalanche-driven vortex rearrangements, which was recently reviewed by Altshuler and Johansen [81]. Much of the work has focused on the avalanches in the context of self-organised criticality (SOC), but while simulations [82, 83, 84] in many cases show the power-law hallmark of SOC, it is more difficult to collect enough experimental data to support a claim of power-law behaviour (but see refs [85, 86, 87]). Altshuler *et al* [88] recently reported robust data showing power-law behaviour in superconducting Nb.

This avalanching behaviour extends the physical picture of the critical state by detailing how the redistribution of flux may occur in superconductors. However, under certain conditions the flux redistribution via avalanches can lead to a runaway process in which the initial gentle flux motion triggers more vigorous motion and eventually develops into an instability. These instabilities, observed already in the early 1960's (see e.g. [89]), are known as flux jumps since they show up in magnetisation mea-

surements as sudden jumps in the curves. The jumps may be complete in the sense that all magnetisation of the superconductor is lost, or they may be incomplete. Sometimes they are seen as periodic features in the magnetisation curves [90]. They are also very abrupt, taking place during a fraction of a second. Clearly, the jumps have dire consequences for high field superconducting magnets, and represents an important design constraint (see e.g Wilson [91] for more details).

4.1 Thermal avalanches

Flux jumps has been explained as thermo-magnetic instabilities by e.g. Swartz and Bean [92], Mints and Rakhmanov [93] and others. Qualitatively the idea involves two central observations: (i) the superconductors exists in the critical state and therefore the current is at its maximal value whereever flux has penetrated; and (ii) motion of flux dissipates heat. In other words, if a small local heating takes place, the temperature T increases slightly to some $T + \delta T$. But at this elevated temperature the critical current $J_c(T)$ has decreased, facilitating further flux motion, which then can release even more heat. We thus have a feedback loop which may result in a runaway process where an ever-increasing temperature induces more vigorous motion of flux until the entire superconductor is filled with flux or some mechanism eventually halts the process. This feedback loop can be averted if the extra heat is transported away fast enough.

The development of thermal instabilities is controlled by the relative importance of diffusion of heat and diffusion of magnetic flux in the superconductor [93]. This can be parametrised by the ratio $\tau = D_t/D_m$ of the thermal and magnetic diffusion constants. For $\tau \ll 1$ flux redistributes much faster than the heat can be carried away, so the superconductor is essentially heated adiabatically as a result of the flux motion: hence this limit is known as the adiabatic limit. For the other extreme $\tau \gg 1$ magnetic flux remains (nearly) fixed during a rapid heating process. In this dynamic limit the heat transfer to the surrounding heat bath is crucial for the stability.

In both cases it is possible to investigate stability criteria for the superconductor by analysing the coupled Maxwell equations

$$\begin{aligned} \nabla \times \mathbf{B} &= \mu_0 \mathbf{J} \\ \nabla \times \mathbf{E} &= -\frac{\partial B}{\partial t} \end{aligned}$$

$$(4.1)$$

and the heat equation

$$c\frac{\partial T}{\partial t} = \kappa\nabla^2 T - \mathbf{E}\cdot\mathbf{J} \tag{4.2}$$

The material constants κ and c are the thermal conductivity and the heat capacity, respectively.

Of particular interest is the applied magnetic field at which the superconductor becomes unstable, the threshold field B_{th}. Expressions for B_{th} have been found in the adiabatic [92] and the dynamic [93, 94] limits for bulk superconductors. The main difference between the two cases is that in the former case B_{th} only depends on intrinsic properties of the superconductor (heat capacity and critical current), whereas in the latter case the ramp rate of the applied field as well as the heat transfer to the surroundings are additional factors entering the equation. This difference can be understood intuitively. In the adiabatic case the avalanche is triggered when a small region is heated to the point where the runaway process starts. Flux then rapidly disperses through the superconducting material, leading to heat dissipation, but the heat does not have time to diffuse during the flux jump. The influence of the external environment is then of limited importance. On the other hand, in the dynamic limit heat is rapidly distributed in the superconductor. As a result, the only way in which the temperature may increase is if the thermal coupling to the surroundings can not remove the heat generated inside the specimen, a situation which may occur as a result of a low heat transfer coefficient or a rapid increase of the applied field.

In thin films the heat coupling to the substrate adds an important source of heat loss even for small τ, which one might expect tends to stabilise the superconductor. However, the concentration of magnetic flux at the edges of a flat specimen, as discussed in section 3.3, acts to destabilise it. The latter effect is usually by far the most important, and thin films are more prone to avalanches than bulk samples.

The flux jumping depends on several material parameters: the heat capacity c, the thermal conductivity κ, and the resistivity ρ, in addition to the heat transfer h to the cold heat bath. All these material constants are strongly temperature dependent at cryogenic temperatures, and hence the flux jumping depends strongly on temperature. One important observation from a technological point of view is the temperature dependence of the threshold field B_{th} in a superconducting slab, which reaches a maximum at some temperature close to $T = 0.8T_c$ [92].
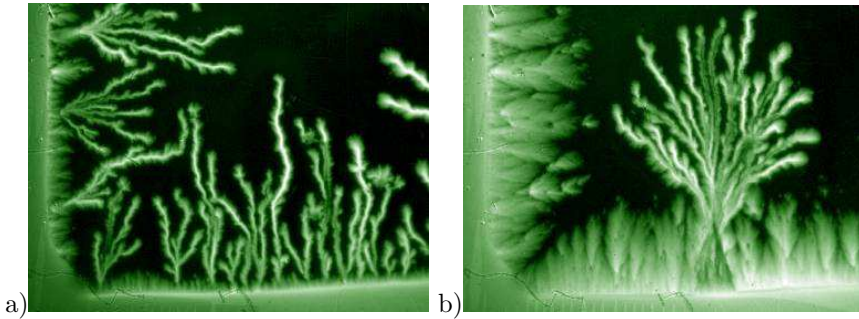
Figure 4.1: Dendritic flux avalanches in MgB$_2$. (a) At low temperature the avalanches are long, narrow and fingerlike. The image was captured at 3.6 K (b) At higher temperature, in this case 9.9 K, the dendrites are tree-like structures.

4.2 Dendritic avalanches

Thermo-magnetic avalanches come in many variants. The main results in this thesis are contained in papers 1 and 2: in them my co-authors and I investigate localised, abrupt avalanches as those depicted in figure 4.1. The figure shows two MO images of the flux distribution at low temperature in a MgB$_2$ superconductor. The most remarkable and prominent feature of these images are the tree-like structures emanating from the sample edges. They are examples of what is known as dendritic or fingerlike avalanches.

The first unequivocal report of this type of flux avalanches dates back to 1993, when Leiderer *et al* [11, 12] triggered them with a point-like heat pulse in YBa$_2$Cu$_3$O$_{7-\delta}$ thin films. They were also observed in Nb by Duran *et al* in 1995, but the phenomenon received little attention until the discovery of superconductivity in MgB$_2$ in 2000. Magnetisation measurements on MgB$_2$ thin films [95] soon revealed that flux jumps were ubiquitous below $T \approx 10$ K: these jumps were later seen in MO experiments [96] displaying structures as the ones shown in figure 4.1. The phenomenon has later been observed in Nb$_3$Sn, YNi$_2$B$_2$C, patterned Pb, and NbN, in all cases thin films [97, 98, 99, 100]. Magnetisation measurements [101] on plain Pb films also hint strongly at dendritic avalanches below $T = 3$ K.

The dendritic avalanches show a rich and complex behaviour. At low temperature they appear frequently, with the tips reaching deeper into the sample as the applied field increases and the Meissner current in the thin film superconductor gets stronger. The detailed pattern is different each time, despite the fact the nucleation sites are fairly reproducible between

independent measurements [102].

The most striking feature is the abruptness of their appearance. Leiderer *et al* [11, 13] measured the propagation velocities of dendrite tips on YBa$_2$Cu$_3$O$_{7-\delta}$ and found $v_{tip} \sim 10^4 - 10^5$ m/s. Similarly in MgB$_2$ they[1] have found $v_{tip} \approx 10^5$ m/s: These propagation velocities are at least an order of magnitude greater than the speed of sound in the materials.

MO experiments have revealed that there exists various stability thresholds for the onset of these avalanches:

- they are restricted to a temperature below some threshold temperature T_{th} [96, 97, 103, 98, 100]

- they occur above a minimum applied magnetic field B_{th} [104, 100]

- the stability depends on sample size [102]

The references in this list include reports on different materials, indicating that these stability thresholds are generic properties of the avalanches. This claim is further supported by reported magnetisation measurements if noise in the $M - H$ curves are interpreted as dendritic avalanches, for example in plain Pb films [101].

It is now agreed by most researchers that the instabilities have a thermomagnetic origin. A recent analysis [105] of the heat equation (4.2) and the Maxwell equations (4.1) showed that for small τ localised, fingerlike instabilities can develop in bulk superconductors; it was later shown that this may also happen in thin films [106]. The analysis on thin strips produced a threshold flux penetration length l_c beyond which the critical state is unstable to nucleation of these localised avalanches. This critical length can be expressed

$$l_c = \frac{\pi}{2} \sqrt{\frac{\kappa}{|J_c'|E}} \left(1 - \sqrt{\frac{2h}{nd|J_c'|E}} \right) \tag{4.3}$$

This expression contains material parameters: the heat transfer coefficient to the substrate h, the creep exponent n (from the creep law equation (3.1)), and the heat conductivity κ. In addition the sample thickness d, and the electric field E enters the equation. While the equation pertains to the thin strip geometry, the concept of a critical penetration length is more general.

In reference [102] we used equation (3.2) to fit observed B_{th} vs sample width w from experiments on MgB$_2$, with l as a fitting parameter. With $l = 82$ μm the agreement between experiments and the theoretical prediction

---
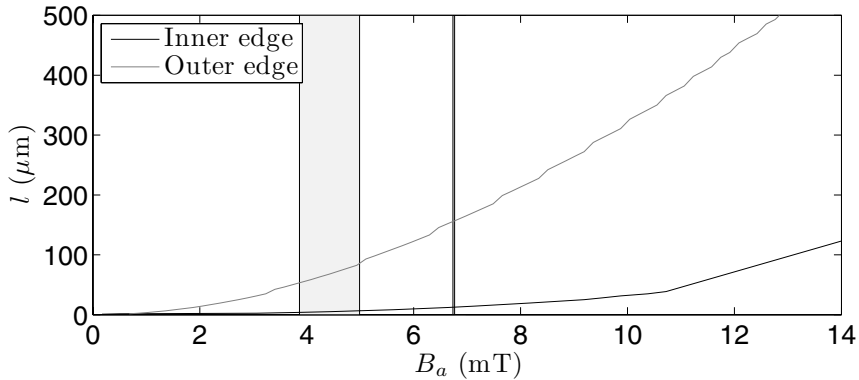
[1]Leiderer, private communication

Figure 4.2: Penetration length l from the inner and outer edge of a superconducting critical state ring computed from the simulations described in section 3.4. The dimensions and critical current value are taken from the sample studied in paper 2.

was excellent. One important consequence of equation (3.2) is that the stability of the strip is improved as the width is reduced; in fact, when $w = l_c$ the threshold field diverges, implying that superconductors with $w < l_c$ are stable. Furthermore, B_{th} as obtained from the combination of equations (4.3) and (3.2) implicitly depends on T via the temperature dependence of n, h and κ. This B_{th} vs T relation diverges at some threshold temperature T_{th}, implying also that there exists a threshold temperature T_{th} above which no dendrites occur. The B_{th} vs T relationship was also found to agree well with experiments, this time on Nb in addition to MgB$_2$.

With the aid of the simulation tool described in section 3.4, the threshold length l_c can help to understand an experimental observation from paper 1 in a more formal way. It was pointed out in the paper that anti-flux dendrites never nucleate spontaneously at the inner edge, but must be triggered by flux dendrites. The penetration lengths l_{outer} and l_{inner} of flux can be calculated as a function of applied field from both ring edges. Shown in figure 4.2 is a plot of the results for such a simulation using the dimensions and the critical current (measured above T_{th} and extrapolated from the linear relationship $J_c = J_{c0}(1 - T/T_c)$) of the MgB$_2$ ring studied in paper 2. Also shown are observed first jump fields at the outer edge (the shaded area) and first perforation fields (the vertical line at ≈ 6.5 mT). Clearly the first perforation event occurs before the critical penetration length is reached at the inner edge. From the more systematic study of perforations

in paper 2 it is clear that after the first perforation frequent perforations inject flux into the central hole, increasing the field at the inner edge and preventing it from ever reaching the negative threshold value required for nucleation of dendrites.

Further experimental evidence favouring the thermo-magnetic mechanism is due to Biehler *et al* [13]. With their ultra-fast magneto-optical setup they have measured the propagation velocities of triggered dendrites in $YBa_2Cu_3O_{7-\delta}$. They were also able to deduce a theoretical expression for the propagation velocity based on a formalism for thermo-magnetic avalanches in a thin film with an indentation [107], and found close agreement with their experiments.

It has also been observed that a thin metal layer deposited on top of the superconductor mitigates the problem of dendritic avalanches [108, 98, 109]. This observation may also be interpreted as a vindication of the thermo-magnetic mechanism since some of the heat generated by flux motion can be carried away in the metal film. One should keep in mind, however, that the rapid propagation of flux associated with an avalanche also induce strong electric fields in the metal layer, which induces dissipative currents there. This amounts to a purely electromagnetic stabilisation, which may or may not be the most important.

The morphology of the structures is a further striking feature, the temperature dependence of which is illustrated in figure 4.1. When T is well below T_{th} the typical shape is long and fairly straight fingers, each of which contains a modest amount of flux. As the temperature approaches T_{th} the individual avalanches become wider, they branch more, and they contain larger amount of flux. This evolution was quantified in reference [100] in terms of a fractal dimension, which increases as the temperature approaches the threshold value. The origin of the branching is still not understood in detail. Simulations [110, 111] suggest that it may arise as a result of the non-local magnetic interaction found in thin films, as discussed in sections 2.5 and 3.3.

Chapter 5

Summary

Most of the work presented in this thesis relates to dendritic avalanches in MgB_2 rings. In superconducting rings anti-flux penetrates from the inner edge while flux penetrates from the outer edge. The most intriguing aspect of the ring geometry is related to the fact that dendrites can span the entire ring width and inject flux into the central hole. Paper 2 is devoted to this injection process entirely. We found that a model of the dendrite as a narrow, heated (and therefore resistive) channel can explain the observed features of the flux injection: (i) that the current distribution changes, (ii) that the total current is affected less than the hole flux, and (iii) that the flux inside the superconducting material is left unaffected by the injection. Most importantly, the model allowed a quantitative estimate of the dendrite temperature, which we found to be $T = 105$ K, and the duration of the process, found to be $\delta t \approx 4 \cdot 10^{-7}$ s (see appendix B for some discussion on the estimates).

Paper 1 is devoted to the observation of several new qualitative features of dendritic instabilities when they occur in rings:

- Anti-flux dendrites are triggered by flux dendrites

- Triggered anti-flux dendrites more or less trace the spine of the dendrite that triggered them

- Flux dendrites may inject large amounts of flux into the ring hole

- Flux dendrites may stop close to the inner edge and increase the negative field in a small region near the dendrite tip

- Highly complex patterns of intertwined flux and anti-flux fingers can occasionally be seen

From experimental data acquired by Pål Erik Goa, I also present some results on single vortex dynamics. Observations of single vortices entering a superconductor is presented in paper 3. The entry is characterised by a narrow band near the edge free of vortices. New vortices nucleate at the edge, but moves quite fast past the vortex free band. The situation persists up to some applied field at which vortices rush into the sample in large numbers, and the initial free band disappears. It is natural to interpret the result in terms of the geometric barrier, which for small fields delay entry of vortices. At some applied field the barrier is overwhelmed by the screening current and large numbers of vortices enters.

The last single vortex paper, paper 4, was initiated by the desire to understand an apparent paradoxical observation, namely that the experiments indicated that domain walls seemed to attract vortices of opposite polarity. This is difficult to reconcile with the simplest picture of a Bloch wall as a long bar magnet. The explanation was found when considering the contribution of the in-plane magnetised domains as well. My contribution to that work was in identifying the problem, helping with image interpretations, and in initial discussions.

Appendix A

Extracting vortex locations

The experimental images of single vortices presented in the edge penetration paper, number 3, are actually frames in a video sequence. As part of an extended analysis of the data I implemented an algorithm for automatically extracting positions of vortices in images, with the intention of tracking their motion. Unfortunately it turned out that the data could not support any interesting conclusions, and the algorithm is thus not directly used in any of the work presented in this thesis. It is nevertheless presented here for reference.

A byproduct of the implementation of the algorithm was a graphical user interface implemented in Matlab which allowed the user to set filter parameters, remove misidentified vortices manually, or add overlooked vortices. This system was used in the work for paper 4, and was one of my contributions in that paper.

The basic problem can be formulated as a search for local maxima in images, which is fairly easy if those maxima are well defined. However, in the single vortex images the signal only marginally stands out from background noise, which complicates the task. The first approach is to use an algorithm due to Crocker and Grier [112]. It consists of the following stages:

- Reduce shot noise via a filter

- Dilate the filtered image

- Identify pixels in the filtered and diluted images which have the same intensity value

Dilation ↓
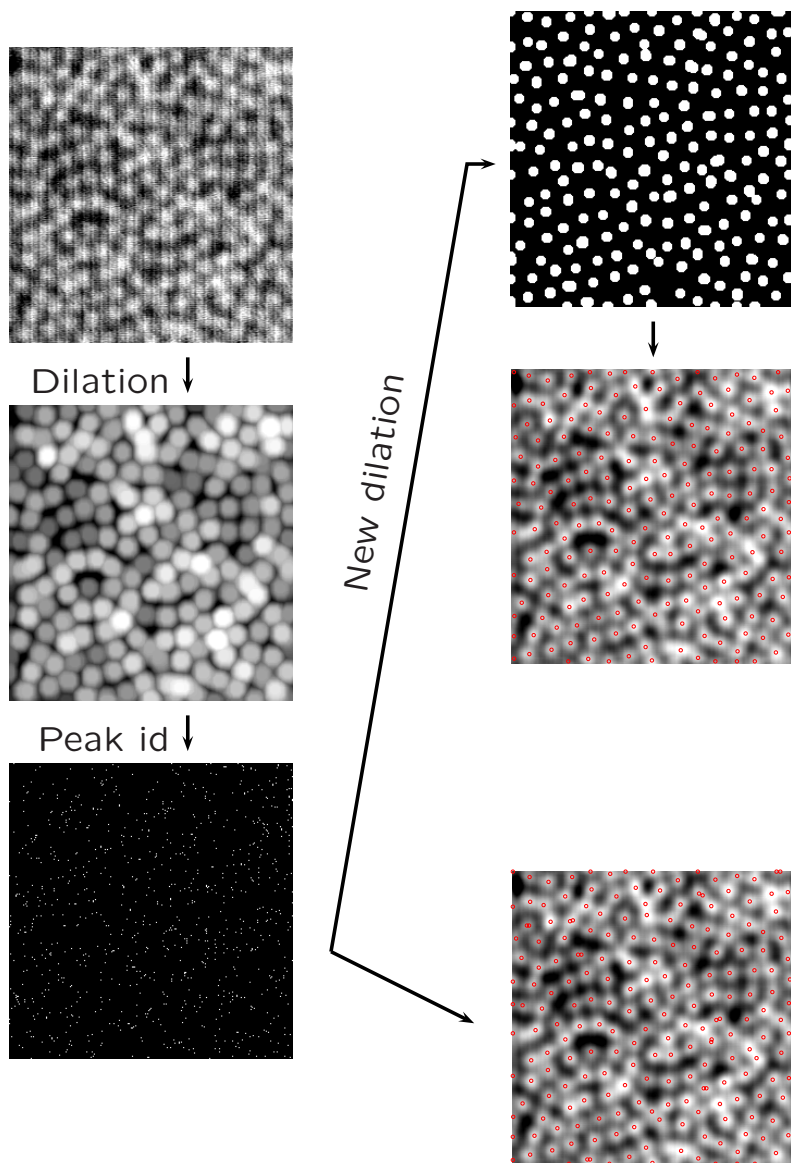
Peak id ↓

New dilation

Figure A.1: Images showing the progress of the algorithm for automated detection of local maxima.

Dilating a gray scale image is a pixel-wise operation which replaces a pixel value with the maximum intensity value in a neighbourhood around the pixel. Such neighbourhoods may take any form, but for the particular problem at hand the neighbourhood should have a size and shape which roughly reflects the size and shape of the vortices. The same applies to the filtering operation. Therefore, I have used a gaussian filter with a size determined by the apparent size of the vortices, and a circular neighbourhood region for the dilation operation with a size equal to the filter size. This size is an input parameter.

Figure A.1 shows an example of the use of the algorithm, with intermediate steps shown. The first stages are shown on the left: the original image is dilated, and a binary map of the pixels equal in the dilated and the filtered images is constructed. At this point the next step depends on the user, which may accept the points as they are, or subject the binary map to a second dilation. Subsequently extracting the centroids of clusters results in a new set of positions. The second dilation operation has the effect of merging close points.

Appendix B

The temperature estimate

The temperature estimation of the dendrite core temperature performed in paper 2 involves some simplifications and uncertainties. This begs some discussion on how the different assumptions affect the temperature estimate. A coarse summary of the assumptions is the following:

- We disregard heat conduction into the superconductor, the κ term in equation (4.2)

- We assume that we have reasonable values for the material parameters entering the formula used to estimate the temperature

- We assume a narrow ring, or at least one in which the current density is reasonably uniform

This appendix discusses some of the issues surrounding the uncertainty of the estimate.

B.1 Material parameters

Under the assumption that we could disregard the heat flow into the superconducting material the equation for the peak temperature was found to be

$$\frac{\rho J^2 d T_c^3}{h_0} = T_{max}^3 (T_{max} - T_0) \tag{B.1}$$

The first point to note from this equation is that the temperature dependence has been collected on the right hand side, and that this fourth order

function in temperature is monotonically increasing for $T > T_0$. It is then clear that the equation has a unique solution for $T > T_0$. It is also possible to show mathematically that this is a maximum value by differentiating the original heat equation with respect to time, but there is a simple physical argument which also leads to the same conclusion: since there is only one extremal point, this must be a maximum if the temperature is bounded.

However, the exact value depends on the constant on the left hand side, let us call it $K = \rho J^2 d T_c^3 / h_0$ for convenience. Among them I expect that J, T_c and d are known to a reasonably high accuracy. The main uncertainty lies with ρ and h_0. While it seems reasonable to expect that previous measurements on identical samples, h_0 from ref [102] (found as a fitting parameter) and ρ from [113] are applicable also on the sample in question, there are some important issues to be aware of. Firstly, the experiments in [102] were not designed to measure h_0, and do not represent the most sensitive measurement of this constant. Secondly, ρ is not entirely temperature independent in the relevant range above T_c (up to about $T = 100$ K), and was also chosen to be a little higher in paper 2 than the measurements in ref [113] indicate. In part this was done to accomodate other resistivities reported on MgB_2 films [114].

One fortunate property of equation (B.1) is that it has a rather steep growth around $T = 100$ K, which means the temperature found from the equation does not depend very strongly on changes in K. As an illustration, let us calculate temperatures for $K_1 = 0.5K$ and $K_2 = 2K$: the result is $T_1 = 90$ K and $T_2 = 124$ K. Of course, if this is taken as the error bounds on the estimate it is far from any exact measurement, but I think it remains an intriguing estimate, and the value $T = 100$ K seems like a reasonable temperature to find inside the dendrite cores.

B.2 Heat loss to the superconductor

Ignoring the heat conduction into the neighbouring region of the superconducting material may seem drastic, as one expects this be a much faster heat diffusion process than the heat loss through the boundary to the substrate. However, as the area of the heated region grows, the heat loss to the substrate is expected to become more important: indeed, by estimating the width of the heated region as the size of the dendrite core, roughly 10 μm, the contact area between the heated channel and the substrate is about 20 times the cross sectional area of the ring, and hence heat is lost to the substrate through an area 10 times larger then the area where heat can escape to the surrounding superconducting material.

Also taking into account the heat conduction term would lower our

temperature estimate. On the other hand, the exact value of the heat conductivity is not known, which itself is an uncertainty. Moreover, a complete simulation of the heating process would also require a resistivity in superconducting state, which follows a highly complicated temperature dependence.

B.3 The narrow ring assumption

The way the assumption of a narrow ring affects the estimate is more difficult to assess. As shown in the paper the current change is distributed unevenly in the ring. One possible scenario is that one has a lower temperature in the part of the heated channel which is deep inside the Meissner region, since there the current is smaller. On the other hand, it seems that the time which the channel is heated should be the same across the ring width: the moment part of the heated channel allows supercurrents to flow again, one would expect the current in the ring to predominantly flow in that superconducting part, thus reducing (or completely removing) the heat dissipation in those parts of the channel that remain at high temperature. For this reason, I would expect the heat dissipation to be distributed more or less evenly across the ring width, and hence the assumption of a uniform current distribution inside the channel is not such a crude simplification.

This discussion makes it clear that there are many uncertainties in the temperature estimate. However, at least it hints strongly at a temperature above T_c inside the core, since even though most of the effects discussed would tend to lower the estimate it takes a significant reduction in K to bring the temperature below T_c. Finally, provided the temperature is above T_c, the duration estimate of $\delta t = 4 \cdot 10^{-7}$ s is not strongly affected by the temperature because the resistivity is almost temperature independent.

Bibliography

[1] E. Salpietro, Superconductor Science and Technology 19 (3) (2006) S84–S89.
URL `http://stacks.iop.org/0953-2048/19/S84`

[2] H. W. Neumüller, W. Nick, B. Wacker, M. Frank, G. Nerowski, J. Frauenhofer, W. Rzadki, R. Hartig, Superconductor Science and Technology 19 (3) (2006) S114–S117.
URL `http://stacks.iop.org/0953-2048/19/S114`

[3] P. B. Alers, Phys. Rev. 105 (1) (1957) 104–108.

[4] H. KIRCHNER, Physics letters. A A 26 (1968) 651.

[5] C. Jooss, J. Albrecht, H. Kuhn, H. Kronmüller, S. Leonhardt, Reports on Progress in Physics 65 (2002) 651.

[6] M. V. Indenbom, V. I. Nikitenko, A. A. Polyanskii, V. K. Vlasko-Vlasov, Cryogenics 30 (1990) 747–749.

[7] R. J. Wijngaarden, K. Heeck, M. Welling, R. Limburg, M. Pannetier, K. van Zetten, V. L. G. Roorda, A. R. Voorwinden, Review of Scientific Instruments 72 (6) (2001) 2661–2664.
URL `http://link.aip.org/link/?RSI/72/2661/1`

[8] A. Soibel, E. Zeldov, M. Rappaport, Y. Myasoedov, T. Tamegai, S. Ooi, M. Konczykowski, V. B. Geshkenbein5, Nature 406 (2000) 282–287.

[9] M. R. Freeman, Phys. Rev. Lett. 69 (11) (1992) 1691–1694.

[10] B. Biehler, U. Bolz, B.-U. Runge, P. Leiderer, Magneto-optic investigation of magnetic flux penetration on a nanosecond timescale, in: T. H. Johansen, D. V. Shantsev (Eds.), Magneto-Optical Imaging,

Vol. 142 of NATO Science Series - II. Mathematics, Physics and Chemistry, Kluwer Academic Publishers, 2004, pp. 47–52.

[11] P. Leiderer, J. Boneberg, P. Brüll, V. Bujok, S. Herminghaus, Physical Review Letters 71 (1993) 2646.

[12] V. Bujok, P. Brüll, J. Boneberg, S. Herminghaus, P. Leiderer, Applied Physics Letters 63 (1993) 412.

[13] B. Biehler, B.-U. Runge, P. Leiderer, R. G. Mints, Physical Review B 72 (2005) 024532.

[14] P. E. Goa, H. Hauglin, A. A. F. Olsen, D. Shantsev, T. H. Johansen, Applied Physics Letters 82 (1) (2003) 79–81.
URL http://link.aip.org/link/?APL/82/79/1

[15] L. E. Helseth, T. M. Fischer, T. H. Johansen, Phys. Rev. Lett. 91 (20) (2003) 208302.

[16] L. E. Helseth, P. E. Goa, H. Hauglin, M. Baziljevich, T. H. Johansen, Phys. Rev. B 65 (13) (2002) 132514.

[17] G. Carneiro, E. H. Brandt, Phys. Rev. B 61 (9) (2000) 6370–6376.

[18] J. Pearl, Journal of Applied Physics 37 (1966) 4139–4141.

[19] D. A. Huse, Physical Review B 46 (1992) 8621–8623.

[20] M. C. Marchetti, Physica C 200 (1992) 155–166.

[21] P. E. Goa, H. Hauglin, Å. A. F. Olsen, M. Baziljevich, T. H. Johansen, REVIEW OF SCIENTIFIC INSTRUMENTS 74 (2003) 141.

[22] M. Terao, Y. Tokunaga, M. Tokunaga, T. Tamegai, Physica C: Superconductivity 426-431 (2005) 94–98.

[23] M. Tokunaga, T. Tamegai, T. H. Johansen, Physica C: Superconductivity 437-438 (2006) 331–335.

[24] B. J. Roth, N. G. Sepulveda, J. John P. Wikswo, Journal of Applied Physics 65 (1) (1989) 361–372.
URL http://link.aip.org/link/?JAP/65/361/1

[25] E. H. Brandt, Physical Review B (Condensed Matter and Materials Physics) 72 (2) (2005) 024529.
URL http://link.aps.org/abstract/PRB/v72/e024529

[26] R. Doll, M. Näbauer, Phys. Rev. Lett. 7 (2) (1961) 51–52.

[27] B. S. Deaver, W. M. Fairbank, Phys. Rev. Lett. 7 (2) (1961) 43–46.

[28] N. Byers, C. N. Yang, Phys. Rev. Lett. 7 (2) (1961) 46–49.

[29] B. Dam, J. M. Huijbregtse, F. C. Klaassen, R. C. F. van der Geest, G. Doornbos, J. H. Rector, A. M. Testa, S. Freisem, J. C. Martinez, B. Stauble-Pumpin, R. Griessen, Nature 399 (1999) 439–442, 10.1038/20880.
URL http://dx.doi.org/10.1038/20880

[30] C. Navau, A. Sanchez, E. Pardo, D.-X. Chen, E. Bartolome, X. Granados, T. Puig, X. Obrados, Physical Review B 71 (2005) 214507.

[31] M. Tomita, M. Murakami, Nature 421 (2003) 517–520, 10.1038/nature01350.
URL http://dx.doi.org/10.1038/nature01350

[32] J. R. Hull, Superconductor Science and Technology 13 (2000) R1.

[33] A. A. Abrikosov, Soviet Physics JETP 5 (1957) 1174–1182.

[34] U. Essmann, H. Träuble, Physics Letters 24A (1967) 526–527.

[35] N. V. Sarma, J. R. Moon, Phil. Mag. 16 (1967) 433–445.

[36] F. Bitter, Physical Review 38 (1931) 1903–1905.

[37] T. Matsuda, K. Harada, H. Kasai, O. Kamimura, A. Tonomura, Science 271 (5254) (1996) 1393–1395.

[38] K. Harada, T. Matsuda, H. Kasai, O. Kamimura, A. Tonomura, Ultramicroscopy 67 (1–4) (1997) 133–141.

[39] S. J. Bending, Advances in Physics 48 (1999) 449–535.

[40] L. Y. Vinnikov, J. Karpinski, S. M. Kazakov, J. Jun, J. Anderegg, S. L. Bud'ko, P. C. Canfield, Physical Review B (Condensed Matter and Materials Physics) 67 (9) (2003) 092512.
URL http://link.aps.org/abstract/PRB/v67/e092512

[41] A. I. Larkin, Y. N. Ovchinnikov, Journal of Low Temperature Physics 34 (1979) 409–428.

[42] L. Balents, M. C. Marchetti, L. Radzihovsky, Physical Review B 57 (1998) 7705–7739.

[43] F. Pardo, et al., Nature 396 (1998) 348–350.

[44] P. Kim, et al., Physical Review B 60 (1999) 12589–12592.

[45] A. Duarte, E. Fernandez Righi, C. A. Bolle, F. de la Cruz, P. L. Gammel, C. S. Oglesby, E. Bucher, B. Batlogg, D. J. Bishop, PRB 53 (17) (1996) 11336–11339.

[46] F. Pardo, F. de la Cruz, P. L. Gammel, E. Bucher, C. Ogelsby, D. J. Bishop, PRL 79 (7) (1997) 1369–1372.

[47] M. V. Marchevsky, Magnetic decoration study of the vortex lattice in superconductors, Ph.D. thesis, Leiden University (1997).

[48] M. Marchevsky, J. Aarts, P. H. Kes, Physical Review B 60 (1999) 14601–14604.

[49] W. Henderson, E. Y. Andrei, M. J. Higgins, PRL 81 (11) (1998) 2352–2355.

[50] Z. L. Xiao, E. Y. Andrei, M. J. Higgins, PRL 83 (8) (1999) 1664–1667.

[51] E. Y. A. Z. L. Xiao, M. J. Higgins, Physical Review Letters 83 (1999) 1664–1667.

[52] C. P. BEAN, RMP 36 (1) (1964) 31–39.

[53] P. W. ANDERSON, Y. B. KIM, Rev. Mod. Phys. 36 (1) (1964) 39–43.

[54] Y. Yeshurun, A. P. Malozemoff, A. Shaulov, Rev. Mod. Phys. 68 (3) (1996) 911–949.

[55] J. R. Thompson, K. D. Sorge, C. Cantoni, H. R. Kerchner, D. K. Christen, M. Paranthaman, Superconductor Science and Technology 18 (7) (2005) 970–976.
URL http://stacks.iop.org/0953-2048/18/970

[56] Y. Otani, B. Pannetier, J. P. Nozieres, D. Givord, Journal of Magnetism and Magnetic Materials 126 (1993) 622–625.

[57] Y. Fasano, et al., Physical Review B 60 (1999) 15047–15050.

[58] R. P. Huebner, Magnetic Flux Structures in Superconductors, Springer-Verlag, 1979.

[59] C. A. Bolle, P. L. Gammel, D. G. Grier, C. A. Murray, D. J. Bishop, D. B. Mitzi, A. Kapitulnik, Phys. Rev. Lett. 66 (1) (1991) 112–115.

[60] P. L. Gammel, D. J. Bishop, J. P. Rice, D. M. Ginsberg, Phys. Rev. Lett. 68 (22) (1992) 3343–3346.

[61] A. M. Grishnin, A. Y. Martynovich, S. V. Yampol'skii, Soviet Physics JETP 70 (1990) 1089–98, translated from Russian.

[62] B. I. Ivlev, N. B. Kopnin, Physical Review B 44 (1991) 2747–2750.

[63] C. P. Bean, J. D. Livingston, Phys. Rev. Lett. 12 (1) (1964) 14–16.

[64] E. Zeldov, A. I. Larkin, V. B. Geshkenbein, M. Konczykowski, D. Majer, B. Khaykovich, V. M. Vinokur, H. Shtrikman, Phys. Rev. Lett. 73 (10) (1994) 1428–1431.

[65] E. H. Brandt, Physica C 332 (2000) 99–107.

[66] Y. Paltiel, et al., Nature 403 (2000) 398–401.

[67] A. A. Elistratov, D. Y. Vodolazov, I. L. Maksimov, J. R. Clem, Phys. Rev. B 66 (2002) 220506.

[68] W. T. Norris, Journal of Physics D: Applied Physics 3 (4) (1970) 489–507.
URL http://stacks.iop.org/0022-3727/3/489

[69] E. H. Brandt, M. Indenbom, Phys. Rev. B 48 (17) (1993) 12893–12906.

[70] E. Zeldov, J. R. Clem, M. McElfresh, M. Darwin, Physical Review B 49 (1994) 9802.

[71] M. Baziljevich, T. H. Johansen, H. Bratsberg, Y. Galperin, P. E. Lindelof, Y. Shen, P. Vase, Physica C 266 (1996) 127.

[72] E. H. Brandt, Physical Review B (Condensed Matter) 49 (13) (1994) 9024–9040.
URL http://link.aps.org/abstract/PRB/v49/p9024

[73] E. H. Brandt, Physical Review B (Condensed Matter) 50 (18) (1994) 13833–13836.
URL http://link.aps.org/abstract/PRB/v50/p13833

[74] E. H. Brandt, Phys. Rev. B 50 (6) (1994) 4034–4050.

[75] E. H. Brandt, Phys. Rev. B 54 (6) (1996) 4246–4264.

[76] E. H. Brandt, Physical Review B 55 (1997) 14513.

[77] E. H. Brandt, Phys. Rev. B 58 (10) (1998) 6506–6522.

[78] E. H. Brandt, J. R. Clem, Physical Review B (Condensed Matter and Materials Physics) 69 (18) (2004) 184509.
URL `http://link.aps.org/abstract/PRB/v69/e184509`

[79] R. M. Ainbinder, G. M. Maksimova, Superconductor Science and Technology 16 (8) (2003) 871–878.
URL `http://stacks.iop.org/0953-2048/16/871`

[80] S. Field, J. Witt, F. Nori, X. Ling, PRL 74 (7) (1995) 1206–1209.

[81] E. Altshuler, T. H. Johansen, RMP 76 (2) (2004) 471.
URL `http://link.aps.org/abstract/RMP/v76/p471`

[82] C. J. Olson, C. Reichhardt, F. Nori, PRB 56 (10) (1997) 6175–6194.

[83] K. E. Bassler, M. Paczuski, PRL 81 (17) (1998) 3761–3764.

[84] K. E. Bassler, M. Paczuski, G. F. Reiter, PRL 83 (19) (1999) 3956–3959.

[85] C. M. Aegerter, Phys. Rev. E 58 (2) (1998) 1438–1441.

[86] C. M. Aegerter, M. S. Welling, R. J. Wijngaarden, EPL 65 (2004) 753–759.

[87] C. M. Aegerter, M. S. Welling, R. J. Wijngaarden, Physica A 347 (2005) 363–374.

[88] E. Altshuler, T. H. Johansen, Y. Paltiel, P. Jin, K. E. Bassler, O. Ramos, Q. Y. Chen, G. F. Reiter, E. Zeldov, C. W. Chu, PRB 70 (14) (2004) 140505.
URL `http://link.aps.org/abstract/PRB/v70/e140505`

[89] P. S. Swartz, C. H. Rosner, Journal of Applied Physics 33 (7) (1962) 2292–2300.
URL `http://link.aip.org/link/?JAP/33/2292/1`

[90] K. Chen, S. W. Hsu, T. L. Chen, S. D. Lan, W. H. Lee, P. T. Wu, Applied Physics Letters 56 (26) (1990) 2675–2677.
URL `http://link.aip.org/link/?APL/56/2675/1`

[91] M. N. Wilson, Superconducting Magnets, Monographs on Cryogenics, Clarendon Press Oxford, 1983.

[92] P. S. Swartz, C. P. Bean, Journal of Applied Physics 39 (1968) 4991.

[93] R. G. Mints, A. L. Rakhmanov, Rev. Mod. Phys. 53 (3) (1981) 551–592.

[94] R. G. Mints, Phys. Rev. B 53 (18) (1996) 12311–12317.

[95] Z. W. Zhao, S. L. Li, Y. M. Ni, H. P. Yang, Z. Y. Liu, H. H. Wen, W. N. Kang, H. J. Kim, E. M. Choi, S. I. Lee, Phys. Rev. B 65 (6) (2002) 064512.

[96] T. H. Johansen, M. Baziljevich, D. V. Shantsev, P. E. Goa, Y. M. Galperin, W. N. Kang, H. J. Kim, E. M. Choi, M.-S. Kim, S. I. Lee, Superconductor Science and Technology 14 (2001) 726.

[97] I. A. Rudnev, S. V. Antonenko, D. V. Shantsev, T. H. Johansen, A. E. Primenko, Cryogenics 43 (2003) 663.

[98] S. C. Wimbush, B. Holzapfel, C. Jooss, Journal of Applied Physics 96 (2004) 3589.

[99] M. Menghini, R. J. Wijngaarden, A. V. Silhanek, S. Raedts, V. V. Moshchalkov, Physical Review B 71 (2005) 104506.

[100] I. A. Rudnev, D. V. Shantsev, T. H. Johansen, A. E. Primenko, Applied Physics Letters 87 (2005) 042502.

[101] S. Hébert, L. Van Look, L. Weckhuysen, V. V. Moshchalkov, Phys. Rev. B 67 (22) (2003) 224510.

[102] D. V. Denisov, D. V. Shantsev, Y. M. Galperin, E.-M. Choi, H.-S. Lee, S.-I. Lee, A. V. Bobyl, P. E. Goa, A. A. F. Olsen, T. H. Johansen, Physical Review Letters 97 (7) (2006) 077002.
URL http://link.aps.org/abstract/PRL/v97/e077002

[103] M. S. Welling, R. J. Westerwaal, W. Lohstroh, R. J. Wijngaarden, Physica C: Superconductivity 411 (2004) 11–17.

[104] F. L. Barkov, D. V. Shantsev, T. H. Johansen, P. E. Goa, W. N. Kang, H. J. Kim, E. M. Choi, S. I. Lee, Physical Review B 67 (2003) 064513.

[105] A. L. Rakhmanov, D. V. Shantsev, Y. M. Galperin, T. H. Johansen, Physical Review B 70 (2004) 224502.

[106] D. V. Denisov, A. L. Rakhmanov, D. V. Shantsev, Y. M. Galperin, T. H. Johansen, Physical Review B 73 (2006) 014512.

[107] R. G. Mints, E. H. Brandt, Phys. Rev. B 54 (17) (1996) 12421–12426.

[108] M. Baziljevich, A. V. Bobyl, D. V. Shantsev, E. Altshuler, T. H. Johansen, S. I. Lee, Physica C 369 (2002) 93.

[109] E. M. Choi, H. S. Lee, H. J. Kim, B. Kang, S. I. Lee, Å. A. F. Olsen, D. Shantsev, T. H. Johansen, Applied Physics Letters 87 (2005) 152501.

[110] T. H. Johansen, M. Baziljevich, D. V. Shantsev, P. E. Goa, Y. M. Galperin, W. N. Kang, H. J. Kim, E. M. Choi, M.-S. Kim, S. I. Lee, Europhysics Letters 59 (2002) 599.

[111] I. S. Aranson, A. Gurevich, M. S. Welling, R. J. Wijngaarden, V. K. Vlasko-Vlasov, V. M. Vinokur, U. Help, Physical Review Letters 94 (2005) 037002.

[112] John Crocker and David Grier, Journal of Colloid and Interface Science 179 (1996) 298–310.

[113] H.-J. Kim, W. N. Kang, E.-M. Choi, M.-S. Kim, K. H. P. Kim, , S.-I. Lee, Physical Review Letters 87 (2001) 087002.

[114] C. B. Eom, M. K. Lee, J. H. Choi, L. J. Belenky, X. Song, L. D. Cooley, M. T. Naus, S. Patnaik, J. Jiang, M. Rikel, A. Polyanskii, A. Gurevich, X. Y. Cai, S. D. Bu, S. E. Babcock, E. E. Hellstrom, D. C. Larbalestier, N. Rogado, K. A. Regan, M. A. Hayward, T. He, J. S. Slusky, K. Inumaru, M. K. Haas, R. J. Cava, Nature 411 (2001) 558.

List of papers

Paper 1 *Flux Dendrites of Opposite Polarity in Superconducting MgB_2 rings observed with magneto-optical imaging*
Åge A. F. Olsen, Tom Henning Johansen, Daniel Shantsev, Eun-Mi Choi, Hyun-Sook Lee, Hyun Jung Kim, Sung-Ik Lee
Physical Review B, 74 (2006), 064506

Paper 2 *Avalanches injecting flux into the central hole of a superconducting MgB_2 ring*
Åge A. F. Olsen, Tom Henning Johansen, Daniel Shantsev, Eun-Mi Choi, Hyun-Sook Lee, Hyun Jung Kim, Sung-Ik Lee
Submitted to Physical Review B

Paper 3 *Single vortices observed as they enter $NbSe_2$*
Åge A. F. Olsen, Harald Hauglin, Tom Henning Johansen, Pål Erik Goa, Daniel Shantsev
Physica C, 408-410 (2004), 537-538

Paper 4 *Interaction between Superconducting Vortices and a Bloch Wall in a Ferrite Garnet Film*
Jørn Inge Vestgården, Daniel Shantsev, Åge A. F. Olsen, Yuri M. Galperin, Vitaliy V. Yurchenko, Pål Erik Goa, Tom Henning Johansen
Physical Review Letters, 98 (2007), 117002

My contribution: important role in identifying the problem to be solved, initial discussions, image interpretation